Stepwise Construction of Silica-supported Tantalum/Iridium Heteropolymetallic Catalysts Using Surface Organometallic Chemistry

Sébastien Lassalle, Ribal Jabbour, Iker Del rosal, Laurent Maron, Emiliano Fonda, Laurent Veyre, David Gajan, Anne Lesage, Chloé Thieuleux, Clément Camp

Stepwise Construction of Silica-supported Tantalum/Iridium Heteropolymetallic Catalysts Using Surface Organometallic Chemistry.

Sébastien Lassalle,[a] Ribal Jabbour,[b] Iker Del Rosal,[c] Laurent Maron,[c] Emiliano Fonda,[d] Laurent Veyre,[a] David Gajan,[b] Anne Lesage,[b] Chloé Thieuleux[a] and Clément Camp*[a]

[a] *Laboratory of Chemistry, Catalysis, Polymers and Processes, C2P2 UMR 5265, Université de Lyon, Institut de Chimie de Lyon, CNRS, Université Lyon 1, CPE Lyon, 43 Bd du 11 Novembre 1918, F-69616 Villeurbanne, France.*
**clement.camp@univ-lyon1.fr*

[b] *Université de Lyon, Centre de RMN à Hauts Champs de Lyon CRMN, FRE 2034, Université de Lyon, CNRS, ENS Lyon, UCB Lyon 1, 69100 Villeurbanne, France.*

[c] *LPCNO (IRSAMC), Université de Toulouse, INSA, UPS, CNRS (UMR 5215); Institut National des Sciences Appliquées, 135 avenue de Rangueil, F-31077 Toulouse, France.*

[d] *Synchrotron SOLEIL, L'Orme des Merisiers, Saint Aubin BP-48, 91192 Gif sur Yvette, France.*

ABSTRACT

A stepwise surface organometallic chemistry (SOMC) methodology consisting in using a silica-supported tantalum species, [(≡SiO)Ta(CH^{t}Bu)(CH$_2$^{t}Bu)$_2$], as a reactive center to coordinate an iridium site, was developed to construct tantalum/iridium heterobimetallic edifices. The resulting material, **MAT-2**, exhibits enhanced catalytic performances - both in H/D isotopic exchange and alkane metathesis reactions - in comparison to **MAT-1**, which was prepared from the direct grafting on silica of a well-defined heterobimetallic Ta/Ir complex. We projected that the difference in catalytic activity was due to the presence of distinct active sites and we used a combination of advanced spectroscopic methods (IR, solid-state NMR and XAS spectroscopies) as well as modeling (computational studies and molecular models) to identify the structure of these surface species. These investigations point towards the presence of three types of active sites at the surface of **MAT-2**: the heterobimetallic surface species, [≡SiOTa(CH$_2$^{t}Bu)$_2${IrH$_2$(Cp*)}] **2-s**, which is also found in **MAT-1**, as well as an unanticipated heterotrimetallic species, [≡SiOTa(CH$_2$^{t}Bu)$_2${IrH$_2$(Cp*)}], **3-s** along with some unreacted monometallic Ta sites [(≡SiO)Ta(CH^{t}Bu)(CH$_2$^{t}Bu)$_2$], **1-s**. The well-defined trimetallic surface species **3-s** was independently prepared and characterized to support this hypothesis. This study highlights the importance of the synthetic methodology used for the preparation of heterobimetallic species through SOMC, and the difficulty to obtain true single-sites surface species.

KEYWORDS

Surface OrganoMetallic Chemistry (SOMC); early/late heterobimetallic species; supported Dual-Atom Catalysts (DACs); hydrogen isotope exchange (HIE); alkane metathesis; hydrides; tantalum; iridium.

1. Introduction

Heterometallic systems attract substantial interest due to their original structures and their capability to promote new chemistry, different from that of their monometallic constituents, through metal-metal synergistic effects.[1–9] Homogeneous approaches are particularly powerful to prepare sophisticated bimetallic complexes featuring a precise and controlled structure. Yet the bottleneck of these systems resides in the use of elaborated on-purpose ligands which are particularly efficient to direct the assembly of the two metals, but can limit their accessibility and therefore their interest in catalysis.[3] Heterogeneous approaches offer numerous advantages, among which the possibility to access low coordinated metallic sites not achievable in solution.[10] However classical heterogeneous systems are generally ill-defined and as a result the exact nature of the catalytically active species often remain elusive which hampers the precise understanding of the cooperative bimetallic mechanisms in place, and thus the rational design of new systems. To address this challenge, surface organometallic chemistry (SOMC) is a method of choice since it allows to generate well-defined surface species from tailored molecular complexes and thus combines the advantages of homogeneous and heterogeneous approaches.[11,12]

Two main synthetic methodologies can be envisioned to prepare well-defined supported heterobimetallic species through SOMC. First, a heterobimetallic complex can be prepared in solution through the condensation of two monometallic precursors. This molecular heterobimetallic derivative can then be grafted onto the solid support in a second step (Scheme 1, route A). This approach was successfully developed in our group recently to prepare original silica-supported Ta-Ir species with excellent performances in catalytic H/D isotope exchange reactions.[10]

Another elegant methodology to access silica-supported heterobimetallic species consists first in grafting an oxophilic monometallic complex onto the oxide support and then, in a second step, in using this supported organometallic species as a reactive center to introduce the second metal, as

summarized in Scheme 1, route B. This strategy has only been explored in very rare instances[13–18] and is different from sequential co-grafting or co-impregnation methods in which both metal sites are orthogonally attached to the support, independently of one another, and are typically converted to supported alloys or nanoparticles after thermal treatment.[19–28][29–32] The purpose of this article is to compare both routes (A and B) in the case of a tantalum-iridium system. We demonstrate that, although homogeneously distributed heterometallic species are formed using both approaches, the nature of the obtained surface species, and therefore the catalytic performances of these materials, are affected by the chosen synthetic methodology. Note that this work falls within the emerging area of research of supported Dual-Atom Catalysts (DACs),[33,34] although the mild SOMC catalyst preparation approach is drastically different from classically used high temperature (750-1200°C) pyrolytic treatment of metal-organic precursors leading to carbon-derived materials containing dual M-M' sites.[35–39]

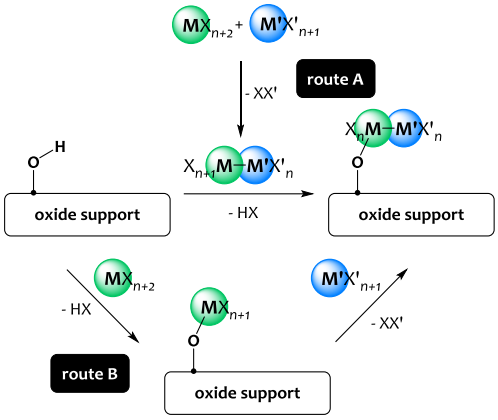

Scheme 1. Methodologies to access heterobimetallic surface species through a SOMC approach.

2. Materials and Methods

2.1 General considerations.

Unless otherwise noted, all reactions and characterization were performed under inert atmosphere either using high-vacuum lines (10^{-5} mBar) Schlenk line techniques or in an MBraun glovebox under an atmosphere of purified argon (<1 ppm O_2/H_2O). Glassware and cannulæ were stored in an oven at ~100 °C for at least 12 h prior to use. Toluene and *n*-pentane were purified by passage through a column of activated alumina, dried over Na/benzophenone, vacuum-transferred to a storage flask and freeze-pump-thaw degassed prior to use. Hexamethyldisiloxane (HMDSO) was refluxed and distilled from CaH_2, freeze-pump-thaw degassed and stored over 4Å molecular sieves prior to use. C_6D_6 was dried over Na/benzophenone vacuum-transferred to a storage flask and freeze-pump-thaw degassed prior to use. Fluorobenzene was freeze-pump-thaw degassed and stored over molecular sieves (4Å) prior to use. Cp*IrH_4,[40] Ta(CH^{t}Bu)(C$H_2{}^t$Bu)$_3$,[41] [(≡SiO)Ta(CH^{t}Bu)(C$H_2{}^t$Bu)$_2$] 1-s,[42,43] and MAT-1,[10] were prepared using literature procedures. The SBA-15 mesoporous silica was synthesized[44] and dehydroxylated[11] at 700°C according to the reported procedures.[10] The preparation of [$(CH_3)_2$CHCH_2]$_7$Si$_8$O$_{12}$OH is detailed in SI and is adapted from a literature procedure.[45] Propane was dried and deoxygenated over freshly regenerated R311G BASF catalyst/molecular sieves (4Å) prior to use. All other reagents were acquired from commercial sources and used as received.

2.2 Syntheses

2.2.1 Synthesis of {(^{i}Bu)$_7$Si$_7$O$_{12}$SiO)}Ta(CH^{t}Bu)(C$H_2{}^t$Bu)$_2$], 1-POSS.

The preparation of **1-POSS** was adapted from a literature procedure.[43] A pentane (8 mL) solution of [$(CH_3)_2$CHCH_2]$_7$Si$_8$O$_{12}$OH (1.460 g, 1.75 mmol) was added dropwise to a dark brown pentane (8 mL) solution of 1 (814 mg, 1.75 mmol). The reaction mixture was stirred 24 hours at room temperature and then 30 min at 60°C yielding a pale yellow solution. The volatiles were removed under vacuum, affording a yellow oil. The crude product was dissolved in the minimum amount of HMDSO and stored at -40°C for 3 days yielding orange crystals of **1-POSS** (1,825 g, 1.48 mmol, 85%). ^{1}H NMR (300 MHz, C_6D_6) δ 4.75 (s, 1H, Ta=C*H*), 2.30 – 1.98 (m, 7H, C*H*(CH_3)$_2$), 1.42 (s, 9H, ^{t}Bu), 1.22 (s, 18H, ^{t}Bu), 1.13 (d, *J* = 6.6 Hz, 18H, *α*- CH(C*H*$_3$)$_2$), 1.07 (m, *J* = 6.6Hz, 24H, *β*- CH(C*H*$_3$)$_2$), 0.90 (d, *J* = 7.0 Hz, 6H, *α*-SiC*H*$_2$), 0.84 (d, *J* = 7.0 Hz, 8H, *β*-SiC*H*$_2$). ^{13}C{^{1}H} NMR (101 MHz, C_6D_6) δ 245.1 (Ta=CHC(CH_3)$_3$), 95.9 (Ta-CH_2), 45.7 (Ta=CHC(CH_3)$_3$), 34.8-34.0 (CH_3), 26.1 (CH_3), 24.4 (CH(CH_3)$_2$), 22.9 (SiCH_2). Elemental analysis calcd (%) for $C_{43}H_{95}O_{13}Si_8Ta$: C 42.13, H 7.81; found: C 42.19, H 7.84.

2.2.2 Synthesis of {(^{i}Bu)$_7$Si$_7$O$_{12}$SiO)}Ta(C$H_2{}^t$Bu)$_2${IrH$_2$(Cp*)}], 2-POSS.

A colorless toluene (8 mL) solution of Cp*IrH_4 (89.5 mg, 0.27 mmol) was added dropwise to an orange toluene (8 mL) solution of **1-POSS** (364 mg, 0.29 mmol). The reaction mixture was stirred 2 hours at room temperature and volatiles were removed *in vacuo* to yield an orange oil. The residue was dissolved in the minimum amount of HMDSO and stored at -40°C overnight to yield red crystals identified as **3-POSS**. The mixture was filtered off to remove **3-POSS** and the filtrate was concentrated and stored at -40°C for 3 days to yield **2-POSS** as red crystals (323 mg, 0.22 mmol, 75%). ^{1}H NMR (300 MHz, C_6D_6) δ 2.31 (s, 15H, Cp*), 2.26 – 2.01 (m, 7H, C*H*(CH_3)$_2$), 1.29 (d, *J* = 14.1Hz, 2H, Ta-CH_2), 1.22 (s, 18H, ^{t}Bu), 1.17 (d, *J* = 6.7 Hz, 18H, *α*-CH(C*H*$_3$)$_2$), 1.10 (d, *J* = 6.6 Hz, 24H, *β*-CH(C*H*$_3$)$_2$), 0.97 (d, *J* = 7.0 Hz, 6H, *α*-SiC*H*$_2$), 0.86 (d, *J* = 7.0 Hz, 8H, *β*-SiC*H*$_2$), 0.18 (d, *J* = 14.1 Hz, 2H, Ta-C*H*$_2$), -11.70 (s, 2H, Ir-*H*). ^{13}C{^{1}H} NMR (101 MHz, THF-*d*$_8$) δ 107.7 (Ta-CH_2), 94.9 (C$_5$Me$_5$), 35.2 (*C*(CH_3)$_3$), 34.01 (*C*(CH_3)$_3$), 26.1-25.7 (CH_3), 24.7 (CH(C*H*$_3$)$_2$), 23.1-23.0 (SiCH_2), 11.0 (C$_5$*Me*$_5$). Elemental analysis calcd (%) for $C_{48}H_{102}IrO_{13}Si_8Ta$: C 38.82, H 6.92; found: C 38.68, H 6.91.

2.2.3 Synthesis of {(^{i}Bu)$_7$Si$_7$O$_{12}$SiO)}Ta(C$H_2{}^t$Bu)$_2${Ir$_2$H$_5$(Cp*)$_2$}], 3-POSS.

A colorless pentane (5 mL) solution of Cp*IrH_4 (50 mg, 0.15 mmol) was added dropwise to an orange pentane (5 mL)

solution of **1-POSS** (93.3 mg, 0.08 mmol). The reaction mixture was stirred for 2 hours at room temperature and the volatiles were removed *in vacuo* to yield an orange oil. The residue was dissolved in the minimum amount of HMDSO and stored at -40°C overnight to yield red crystals identified as **3-POSS** (104 mg, 0.06 mmol, 82%). ^{1}H NMR (300 MHz, C_6D_6) δ 2.20 (s, 7H, C*H*(CH_3)$_2$), 2.14 (s, 30H, Cp*), 1.28 (s, 9H, ^{t}Bu), 1.20 (d, *J* = 6.6 Hz, 18H, *α*-CH(C*H*$_3$)$_2$), 1.12 (m, 24H, *β*-CH(C*H*$_3$)$_2$), 0.93 – 0.89 (m, 6H, *α*-SiC*H*$_2$), 0.88 – 0.82 (m, 8H, *β*-SiC*H*$_2$), -11.02 (s, 5H,Ir-H). ^{13}C{^{1}H} NMR (101 MHz, C_6D_6) δ 93.6 (Ta-*C*H$_2$), 93.6 (*C*$_5$Me$_5$), 35.2-33.3 (*C*(CH$_3$)$_3$), 26.3-25.0 (*C*H$_3$), 24.5 (*C*H(C*H*$_3$)$_2$), 23.2-22.8 (Si*C*H$_2$), 11.1 (C$_5$*Me*$_5$). Elemental analysis calcd (%) for $C_{53}H_{109}Ir_2O_{13}Si_8Ta$: C 36.49, H 6.30; found: C 35.93, H 6.32.

2.2.4 Synthesis of [(CH$_2$^{t}Bu)Ta{Ir$_2$H$_5$(Cp*)$_2$}], 3.

*From [Ta(CH^{t}Bu)(CH$_2$^{t}Bu)$_3$], **1**.*

A colorless pentane solution (10 mL) of Cp*IrH$_4$ (171 mg, 0.52 mmol, 2 eq.) was added dropwise to a dark-brown pentane solution (10 mL) of Ta(CH^{t}Bu)(CH$_2$^{t}Bu)$_3$ (120 mg, 0.26 mmol, 1 eq.). The reaction mixture turned dark orange and was stirred at room temperature for 24h. The volatiles were removed *in vacuo* to yield a red/orange solid (253 mg). The crude product was dissolved in the minimum amount of pentane and stored at -40°C overnight to yield orange needles crystals of **3** (223 mg, 0.23 mmol, 88%). Single crystals suitable for X-ray diffraction were obtained similarly.

From [{Ta(CH$_2$^{t}Bu)$_3$}{IrH$_2$(Cp)}], **2**.*

A colorless pentane solution (8 mL) of Cp*IrH$_4$ (23 mg, 0.07 mmol, 1 eq.) was added dropwise to an orange pentane solution (8 mL) of **2** (50 mg, 0.07 mmol, 1 eq.). The reaction mixture turned dark orange and was stirred at room temperature for 24h. The volatiles were removed *in vacuo* to yield a red/orange solid. The crude product was dissolved in the minimum amount of pentane and stored at -40°C overnight to yield orange needles crystals of **3** (60 mg, 0.06 mmol, 87%). ^{1}H NMR (400 MHz, 293K, C_6D_6) δ 2.11 (s, 30H, Cp*), 1.33 (s, 18H, ^{t}Bu), 0.62 (s, 4H, Ta-CH$_2$), -10.52 (s, 5H, Ir-H). ^{13}C{^{1}H} NMR (101 MHz, 293K, C_6D_6) δ = 107.9 (Ta-*C*H$_2$), 93.3 (*C*$_5$Me$_5$), 35.6 (C(*C*H$_3$)$_3$), 11.0 (C$_5$*Me*$_5$). DRIFT (293K, cm^{-1}) ν = 2949 (s, ν$_{C-H}$), 2898 (s, ν$_{C-H}$), 2854 (s, ν$_{C-H}$), 2734 (m, ν$_{C-H}$), 2084 (s, ν$_{Ir-H}$), 2043 (s, ν$_{Ir-H}$), 2018 (s, ν$_{Ir-H}$), 1996 (s, ν$_{Ir-H}$), 1967 (s, ν$_{Ir-H}$), 1457 (s), 1380 (s), 1353 (s), 1220 (s), 1073 (m), 1069 (m), 1027 (s). Elemental analysis calcd (%) for $C_{30}H_{57}Ir_2Ta$: C 36.65, H 5.84; found: C 36.67, H 5.87.

2.2.5 Synthesis of [{(CH$_2$^{t}Bu)Ta(OSi(O^{t}Bu)$_3$)}{Ir$_2$H$_5$(Cp*)$_2$}], 3-TBS.

A colorless pentane solution of HOSi(O^{t}Bu)$_3$ (13 mg, 0.05 mmol, 1 eq.) was added dropwise to another orange pentane (50 mL) solution of 3 (50 mg, 0.05 mmol, 1 eq.). After 4 hours stirring at r.t. the volatiles were remove under vacuum yielding a light orange crude solid (58 mg). The solid was dissolved in the minimum amount of pentane and stored at -40°C for 3 days yielding crystals of unreacted complex 3. These crystals were filtered off, the filtrate was concentrated by half under vacuum and stored at -40°C for another 3 days yielding 3-TBS as orange crystals (42 mg, 0.03 mmol, 67%). ^{1}H NMR (400 MHz, C_6D_6) δ 2.15 (s, 30H, Cp*), 1.56 (s, 27H, ^{t}Bu), 1.33 (s, 9H, ^{t}Bu), 1.08 (s, 2H, Ta-C*H*$_2$), -11.14 (s, 5H, Ir-H). ^{13}C{^{1}H} NMR (101 MHz, C_6D_6) δ 93.4 (Ta-CH$_2$), 93.3 (*C*$_5$Me$_5$), 72.8 (O*C*(CH$_3$)$_3$), 35.6 (CH$_2$C(*C*H$_3$)$_3$), 34.2 (CH$_2$*C*(CH$_3$)$_3$), 32.1 (OC(*C*H$_3$)$_3$)), 11.2 (C$_5$*Me*$_5$).

2.2.6 Preparation of MAT-2.

Powder [≡SiOTa(CH$_2$^{t}Bu)(CH$_2$^{t}Bu)$_3$], **1-s**, (801 mg, 0.49 mmol Ta, 1 eq.) is charged in one compartment of a two-sided Schlenk reaction vessel equipped with a sintered glass filter and Cp*IrH$_4$ (163 mg, 0.49 mmol, 1 eq.) is placed in the other compartment. The double-Schlenk vessel is then evacuated (10^{-5} mBar) and dry pentane (15 mL) is added in both compartments *via* vacuum distillation. The colorless solution of complex Cp*IrH$_4$ is transferred through the frit to the [≡SiOTa(CH$_2$^{t}Bu)(CH$_2$^{t}Bu)$_3$] powder suspension and stirred at room temperature for 2 h. After the reaction, the pale red supernatant is filtered away from the solid. The solid is washed with fresh pentane and the supernatant is removed again. This procedure is repeated 6 times to ensure removal of any unreacted Cp*IrH$_4$. The volatile components are then condensed in a 6.7 liters round bottom flask, propane (3.2 mmol) is introduced as internal standard and the neopentane evolved during the grafting is quantified by G.C. (0.43 mmol, 0.9 eq). The resulting pale yellow powder is dried under vacuum (10^{-5} mBar) for 2 hours at room temperature to yield 915 mg of **MAT-2**. ^{1}H MAS SSNMR (500 MHz, 293 K) δ = 2.1 (Cp*), 1.0 (CH$_2$^{t}Bu), -11.3 (Ir-H). ^{13}C CPMAS SSNMR (126 MHz, 293 K) δ = 110.4 (Ta-*C*H$_2$), 93.9 (*C*$_5$Me$_5$), 33.5 (^{t}Bu), 9.1 (C$_5$*Me*$_5$). DRIFT (293K, cm^{-1}) ν 2956 (s, ν$_{C-H}$), 2904 (s, ν$_{C-H}$), 2863 (m, ν$_{C-H}$), 2065 (m, ν$_{Ir-H}$), 2020 (s, ν$_{Ir-H}$), 1947 (m, ν$_{Ir-H}$). Elemental analysis calcd (%) for MAT-2: C 12.66, H 2.07, Ir 10.13, Ta 9.54; found: C 12.85, H 2.13, Ir 9.51, Ta 9.72.

2.2.7 Preparation of MAT-3.

SBA-15$_{700}$ (300 mg dehydroxylated at 700°C under 10^{-5} mBar vacuum for 10 hours, 0.24 mmol of OH, 1.0 eq.) is charged in one compartment of a two-sided Schlenk reaction vessel equipped with a sintered glass filter and complex **3** (262 mg, 0.26 mmol, 1.1 eq.) is placed in the other compartment. The double-Schlenk vessel is then evacuated (10^{-5} mBar) and dry pentane (15 mL) is added to **3** *via* vacuum distillation. The intense red solution of complex **3** is transferred through the frit to the SBA-15$_{700}$ powder and stirred at room temperature for 2 h upon which time the material turns pale yellow. After the reaction the pale red supernatant is filtered away from the solid. The solid is washed with fresh pentane and the supernatant is removed again. This procedure is repeated 6 times to ensure removal of any unreacted **3**. The volatile components are then condensed in a 6.7 liters round bottom flask, propane (3.5 mmol) is introduced as internal standard and the neopentane evolved during the grafting is quantified by G.C. (0.20 mmol, 0.9 eq). The resulting pale yellow powder is dried under vacuum (10^{-5} mBar) for 2 hours at room temperature to yield 420 mg of compound **MAT-3**. ^{1}H MAS SSNMR (500 MHz, 293 K) δ 2.1 (Cp*), 0.9 (CH$_2$^{t}Bu), -11.3 (Ir-H). ^{13}C CPMAS SSNMR (126 MHz, 293 K) δ 93.2 (C$_5$Me$_5$), 33.1 (^{t}Bu), 9.2 (C$_5$*Me*$_5$). DRIFT (293K, cm^{-1}) ν 2951 (s, ν$_{C-H}$), 2911 (s, ν$_{C-H}$), 2864 (s, ν$_{C-H}$), 2030 (s, ν$_{Ir-H}$), 1947 (s, ν$_{Ir-H}$), 1865 (s, δ$_{C-H}$).

Elemental analysis calcd (%) for MAT-3: C 10.84, H 1.67, Ir 13.88, Ta 6.53; found: C 11.12, H 1.79, Ir 13.80, Ta 6.45.

2.3 Catalysis

2.3.1 Hydrogen-deuterium catalytic exchange reaction using C_6H_5F as substrate and C_6D_6 as deuterium source.

In a typical experiment, **MAT-2** (7.7 mg, 0.004 mmol of Ta) was charged in a J. Young NMR tube and suspended in a stock solution composed of fluorobenzene (6.6 mg, 0.069 mmol), hexamethyldisiloxane (6.0 mg, 0.037 mmol) as internal standard and C_6D_6 (0.58 mL). The NMR tube was sealed under argons and the reaction was then heated at 70°C inside a NMR spectrometer and periodically monitored by ^{1}H NMR and ^{19}F NMR spectroscopy. The monitoring of the catalytic activity was realized on independently prepared catalysts with excellent reproducibility.

2.3.2 Split test

MAT-2 (10.5 mg, 0.0056 mmol Ta) was charged in a J. Young NMR tube and suspended in a stock solution of fluorobenzene (9.0 mg, 0.094 mmol) and hexamethyldisiloxane (6.4 mg, 0.039 mmol) as internal standard in C_6D_6 (0.58 mL). The NMR tube was sealed under argon and the solution was heated in a 70 ± 2°C silicone oil bath and periodically monitored by ^{1}H NMR and ^{19}F NMR spectroscopy. After 3 hours reaction (30% conversion) the supported catalyst was removed by filtration through a dry glass microfiber filter under argon and the filtrate was transferred into another J. Young NMR tube which was again heated in a 70 ± 2°C silicone oil bath and periodically monitored by ^{1}H NMR and ^{19}F NMR spectroscopy. No further conversion (30%) of fluorobenzene was observed after 48 hours. Analysis of this liquid filtrate by ICP-MS showed undetectable amount of Ta and Ir metals in solution (below detection limit <0.001 wt% Ir, <0.001 wt% Ta). Analysis of the spent solid catalyst by TEM showed good integrity of the material structure with the absence of metal nanoparticles and a homogeneous distribution of Ta and Ir in equimolar ratio as seen by EDX.

2.3.3 Catalyst reuse

MAT-2 (10.5 mg, 0.0056 mmol Ta) was charged in a J. Young NMR tube and suspended in a stock solution of fluorobenzene (9.0 mg, 0.094 mmol) and hexamethyldisiloxane (5.5 mg, 0.034 mmol) as internal standard in C_6D_6 (0.57 mL). The NMR tube was sealed under argon and the solution was heated in a 70 ± 2°C silicone oil bath and periodically monitored by ^{1}H NMR and ^{19}F NMR spectroscopy. After 24 hours reaction (96.0% conversion) the NMR tube was transferred to the Ar atmosphere glovebox. Fluorobenzene (9.0 mg, 0.094 mmol) was added to the NMR tube which was again heated in a 70 ± 2°C silicone oil bath. After 24 hours reaction, 92.4% conversion was reached. Initial TOFs were identical for run#1 and run#2 (1.59 h^{-1} and 1.56 h^{-1} respectively) showing good reuse of the catalyst without deactivation (see Figure S31).

2.3.4 Propane metathesis catalysis.

In a typical experiment, **MAT-2** (52 mg, 0.027 mmol of Ta) was charged in a 500 mL batch reactor under argon. After evacuation of the gas phase, propane (730 mBar, 530 eq.) was introduced and the batch reactor was heated at 200°C. The gas phase was sampled periodically and analyzed by GC to monitor quantity of products and their distribution during the reaction. The turnover number (TON) is calculated as follows: TON = $n_C/(3n_{Ta})$ where n_C is the total number of moles of carbon atoms arising from all the reaction products (methane, ethane, butanes and pentanes) and n_{Ta} is the number of moles of Ta introduced in the experiment.

2.4 Characterizations

2.4.1 IR spectroscopy.

Samples were prepared in a glovebox (diluted in KBr for molecular compounds, pure for silica-supported species), sealed under argon in a DRIFT cell equipped with KBr windows and analyzed on a Nicolet 6700 FT-IR spectrometer.

2.4.2 Elemental analyses.

ICP-MS and combustion analyses were performed under inert atmosphere either at the School of Human Sciences, Science Center, London Metropolitan University or at Mikroanalytisches Labor Pascher, Germany.

2.4.3 X-ray diffraction structural determinations.

Experimental details regarding XRD measurements are provided in SI. CCDC 2018037-2018040 contain the supplementary crystallographic data for this paper. These data are provided free of charge by the Cambridge Crystallographic Data Centre.

2.4.4 NMR Spectroscopy.

Solution NMR spectra were recorded on Bruker AV-300, AVQ-400 and AV-500 spectrometers. Chemical shifts were measured relative to residual solvent peaks, which were assigned relative to an external TMS standard set at 0.00 ppm. ^{1}H and ^{13}C NMR assignments were confirmed by ^{1}H–^{1}H COSY and ^{1}H–^{13}C HSQC and HMBC experiments.

The proton solid-state NMR spectra were obtained on a Bruker 700 MHz narrow-bore spectrometer using a double resonance 2.5 mm MAS probe. The samples were introduced under argon in a zirconia rotor, which was then tightly closed. Ultra-dry nitrogen gas was used to spin the samples to avoid sample degradation. For all the proton multiple-quantum experiments, the spinning frequency was set to 18 kHz. The 2D proton DQ-SQ correlation spectra were recorded according to the following general scheme: excitation of DQ coherences, t_1 evolution and reconversion into observable magnetization, Z-filter, and detection. DQ excitation and reconversion were achieved using the POST-C7 pulse sequence.[46–48] The length of the POST-C7[49] excitation and reconversion block was set to 160 μs (corresponding to seven basic POST-C7 cycles). Quadrature detection in ω_1 was achieved using the States-TPPI method.[50] A recycle delay of 2 s was used. The spectral width in the indirect dimension was set to 70000 Hz. The 2D proton TQ-SQ correlation spectra was recorded according to the following general scheme:

excitation of TQ coherences, t_1 evolution, reconversion into observable magnetization, Z-filter, and detection.[51–55] TQ excitation was achieved by the sequential application of first a 90° proton pulse followed by a DQ POST-C7 pulse sequence as previously described in the literature. The length of the POST-C7 excitation and reconversion block was also set to 160 μs. Quadrature detection in ω_1 was achieved using the States-TPPI method.[50] A recycle delay of 2 s was used and the spectral width in the indirect dimension was 120000 Hz.

2.4.5 X-ray Absorption Spectroscopy.

The samples (in the form of powders) were compacted and sealed under argon in glass capillaries to prevent exposure to air or moisture. The X-ray absorption measurements were performed on the SAMBA beamline at the Synchrotron SOLEIL (Gif sur Yvette, France) in transmission mode. The energy calibration was made *versus* a tantalum foil standard. Data analysis was performed using Demeter software package.[56] The theoretical modelization and fit of the EXAFS spectra within Demeter software were done using corresponding crystallographic and DFT structures.

2.4.6 Computational Details.

All DFT calculations were carried out with the Gaussian 09 suite of programs.[57] Geometries were fully optimized in gas phase without symmetry constraints, employing the B3PW91 functional.[58,59] The nature of the extrema was verified by analytical frequency calculations. The calculation of electronic energies and enthalpies of the extrema of the potential energy surface (minima and transition states) were performed at the same level of theory as the geometry optimizations. IRC calculations were performed to confirm the connections of the optimized transition states. Iridium and Tantalum atoms were treated with a small-core effective core potential (60 MWB), associated with its adapted basis set[60] augmented with a polarization function (ζ_f = 0.938 and 0.790 respectively for Ir and Ta). Si atoms were treated with a Stuttgart effective core potential[61] augmented with a polarization function (ζd = 0.284).[62] For the other elements (H, C and O), Pople's double-ζ basis set 6-31G(d,p) was used.[63–66] The vibrational frequencies were calculated using a scaling factor of 0.9575 as proposed by Irikura et al.[67]

3. Results and discussion

3.1 Materials preparation

We recently reported an efficient and clean synthetic methodology to access original tantalum/iridium heterobimetallic species, based on the alkane elimination reaction between a nucleophilic early metal alkyl/alkylidene derivative Ta(CH^{t}Bu)(CH$_2$^{t}Bu)$_3$, **1**, and a late metal Brønsted acidic hydride, Cp*IrH$_4$, affording the bimetallic complex [{Ta(CH$_2$^{t}Bu)$_3$}{IrH$_2$(Cp*)}], **2** (Scheme 2).[10] Complex **2** was successfully grafted onto silica upon treatment of a SBA-15 silica support dehydroxylated at 700 °C (SBA-15$_{700}$) with a pentane solution of **2**. This led to material **MAT-1** which contains the well-defined silica-supported monopodal surface species [≡SiOTa(CH$_2$^{t}Bu)$_2${IrH$_2$(Cp*)}], **2-s** (Scheme 2).[10]

In order to explore the feasibility of route B, *i.e.* the stepwise construction of supported heterobimetallic edifices directly on silica, we first prepared the monometallic monopodal silica-supported tantalum species [(≡SiO)Ta(CH^{t}Bu)(CH$_2$^{t}Bu)$_2$], **1-s** (Scheme 2), based on previous knowledge from our lab.[42,43] Reaction monitoring by infrared spectroscopy shows that the characteristic sharp band at 3741 cm^{-1} (ν(O-H)) from SBA-15$_{700}$ has completely disappeared in the first step, indicating the full consumption of the isolated surface silanols through grafting of the Ta monometallic precursor (Figure 1). New signals are found at 2960-2860 cm^{-1} and are assigned to ν(C-H) stretches of the neopentyl/neopentylidene ligands from **1-s**. This supported species exhibits the same reactive neopentylidene and neopentyl ligands as those found in **1**, and we thus anticipated analogous alkane elimination reactivity towards acidic iridium hydrides than that leading to the heterobimetallic complex **2** (Scheme 2).

Upon treatment of the monometallic grafted tantalum complex **1-s** with a pentane solution of Cp*IrH$_4$ at room temperature, using a Ta:Ir stoichiometric ratio of 1:1, the pale yellow powder turns immediately into a more intense yellow-colored material, noted **MAT-2**. 0.9 equiv. of neopentane is released *per* surface Ta atom, as titrated by gas chromatography (GC). This analysis is consistent with the chemical reaction of the iridium molecular precursor, Cp*IrH$_4$, with the tantalum surface species **1-s** yielding new Ta/Ir surface species through alkane elimination observed for the preparation of **2** in solution. This is further supported by the IR spectroscopy analysis of **MAT-2**, with the appearance of a new set of bands, assigned to ν(Ir-H) stretches, in the 2080-1940 cm^{-1} region (Figure 1).[68,69] It is worth mentioning that Cp*IrH$_4$ does not react with silica in the absence of Ta (see Figure S30).

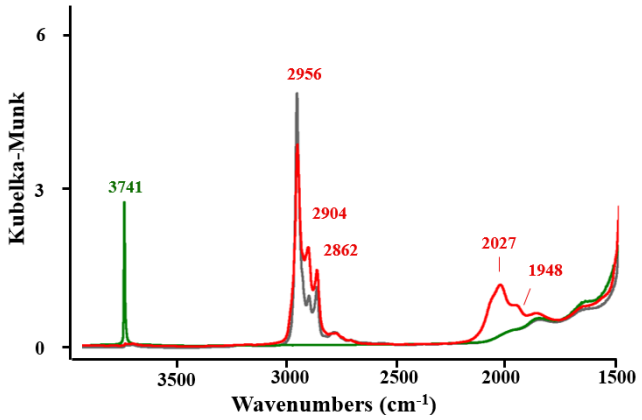

Figure 1. Diffuse Reflection Infrared Fourier Transform spectra of SBA-15$_{700}$ (green line), **1-s** (grey line) and **MAT-2** (red line) recorded on powder materials under argon.

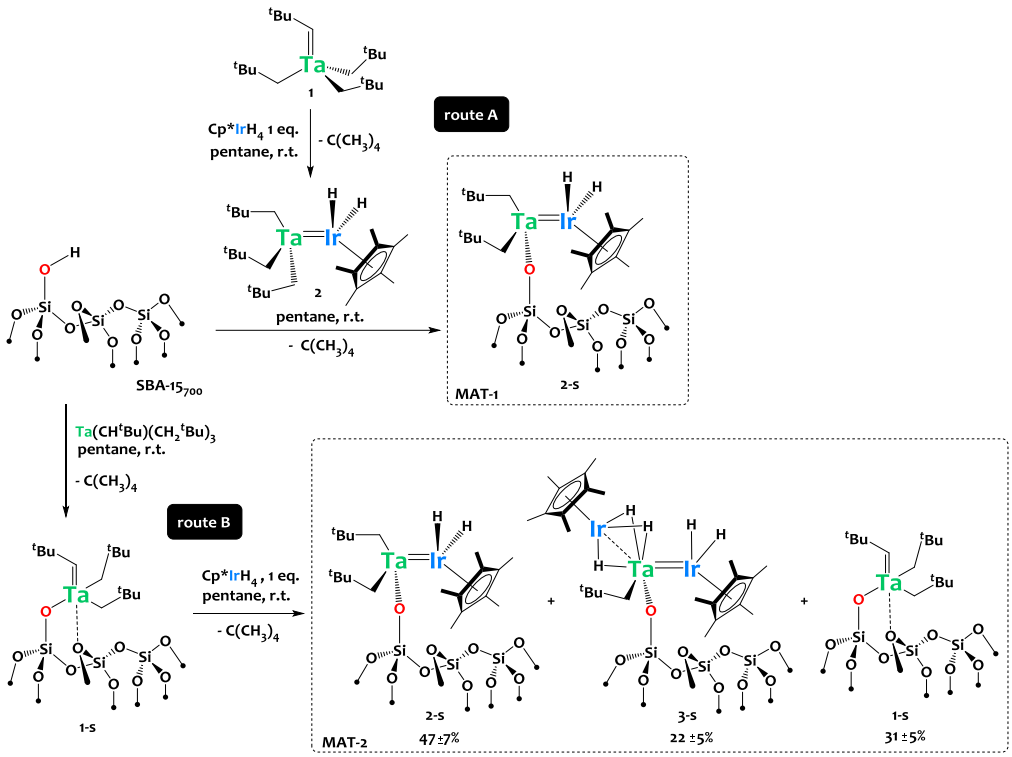

Scheme 2. Preparation of silica-supported species.

The elemental analysis of **MAT-2** (Expected: Ir:Ta ratio = 1.0(1), C:Ta ratio = 20.0(1), Found: Ir:Ta ratio = 0.9(1), C:Ta ratio = 19.7(1)) is similar to that for **MAT-1** (Ir:Ta ratio = 1.0(1), C:Ta ratio = 19.9(1)). The total Ta content in **MAT-2** (4.7 mol%) is analogous to that measured by elemental analysis for the monometallic material **1-s** (4.5 mol%), showing that no, or undetectable negligible amount of Ta was detached from the surface during the preparation of **MAT-2**. Taken together, these analyses suggest that, globally, one iridium center has reacted with one tantalum center in route B. However this is not sufficient to claim that routes A and B are equivalent on a molecular level.

3.2 Catalytic activity

First hints of the dissimilarities between **MAT-1** and **MAT-2** were gained through the analysis of their catalytic performances. As reported by our group, the Ta/Ir sites from **MAT-1** are able to perform catalytic Hydrogen Isotope Exchange (HIE) reactions with excellent performances that rivals those of the best systems reported to date.[10] We thus compared the catalytic HIE activity of **MAT-1** and **MAT-2** in the benchmark H/D scrambling reaction between C_6D_6 and C_6H_5F at 70°C using 6 mol% of Ta. As shown on Figure 2, **MAT-2** exhibits a significant increase in activity (TOF = 1.59 h^{-1}, 95 % conversion in 24 hours) compared to the previously reported material **MAT-1** (TOF = 1.04 h^{-1}, 70% conversion in 24 hours), thereby suggesting the existence of different active species in both materials. Noteworthy, the supported Ta/Ir heteropolymetallic species from **MAT-1** and **MAT-2** both show a substantially enhanced catalytic activity compared to monometallic silica-supported tantalum analogues, such as the alkyl/alkylidene species **1-s** (which is inactive) and the tantalum hydride species [(≡SiO)$_2$TaH$_x$] (TOF = 0.42 h^{-1}, 30% conversion in 24 hours), which were tested as benchmarks for this reaction (Figure 2). This suggests that metal-metal cooperative effects are present and beneficial for catalysis.

In order to assess the robustness of catalyst **MAT-2**, a split test experiment at 30% conversion has been carried out and no evolution of the substrate conversion was observed after filtration of the solid catalyst, showing that there is no active metal species in solution. In addition undetectable amount (below detection limit <0.001 wt%) of both Ta and Ir was observed in the analysis of the liquid phase via ICP-MS, which indicates that no leached inactive metal species are present in solution as well. Analysis of the spent catalyst by TEM shows the absence of metal nanoparticles and EDX shows that the weight percent of Ta and Ir as well as the Ta/Ir ratio before and after catalysis are the same, which further suggests that the catalyst integrity is maintained throughout H/D exchange catalysis.

Furthermore catalyst **MAT-2** reuse has been performed. 96.0% conversion was obtained in the first reaction run (24 hours reaction) and 92.4% conversion was reached in the second reaction run (24 hours reaction). Initial TOFs were identical for run 1 and run 2 (1.59 h^{-1} and 1.56 h^{-1} respectively) showing a good reuse of the catalyst without substantial deactivation (see Figure S31).

Supported tantalum alkyls and hydrides on silica are known to catalyze linear or branched alkanes metathesis.[70,71] Therefore, we have also compared the catalytic activity of **MAT-1** and **MAT-2** in propane metathesis. The tests were carried out at 200°C in a batch reactor with a tantalum loading of 0.1 mol%. The reaction was monitored by GC and GC-MS over time to quantify and identify the reaction products. Here

again, **MAT-2** displayed a significantly enhanced catalytic activity compared to **MAT-1**, with TONs after 40 hours reaction of 118 *vs* 50, and TOFs of 8.3 h^{-1} *vs* 3.2 h^{-1}, respectively (Figure 3). During the initial stage of the reaction we observe the release of neopentane in the gas phase. This suggests that the incoming propane reacts with the surface Ta-neopentyl groups to generate, through sigma-bond metathesis, Ta-propyl moieties and liberate neopentane. This proposed C-H bond activation is typical of surface Ta-alkyl complexes, and is the first step in the reported propane metathesis mechanism with monometallic Ta/SiO_2 species.[71] Methane, ethane, butanes and pentanes account for all of the reaction products with excellent mass balance. No significant difference in product selectivity is observed between **MAT-1** and **MAT-2**: both catalysts are more selective towards C2 (50-60%) and C4 (30-40%) homologues, while C1 and C5 products are formed in lower amounts (below 5%), which is a typical behavior for Ta and W propane metathesis catalysts.[16,19,70–72] Given the similarity in products distribution, a reaction mechanism analogous to that classically accepted for propane metathesis catalyzed by monometallic Ta/SiO_2 active sites is plausible. Note that HRTEM analyses of **MAT-2** prior and after catalysis excluded the formation of metal nanoparticles during the material preparation or in the course of catalysis, which testify the high robustness of the heterometallic surface sites (see SI).

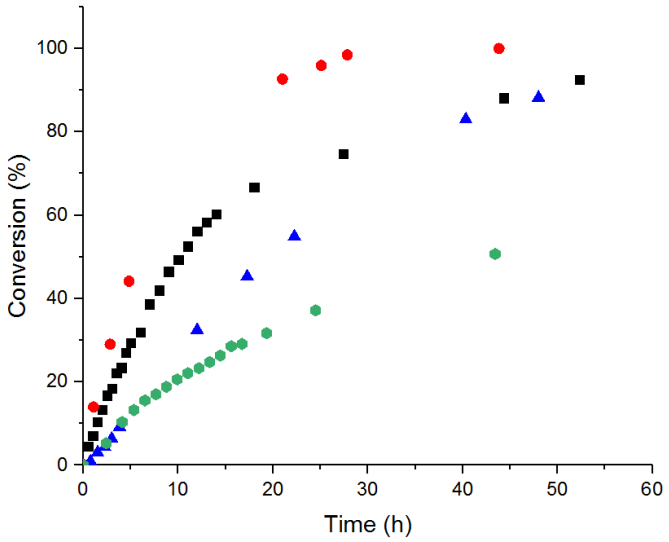

Figure 2. Conversion of fluorobenzene as a function of reaction time. The H/D exchange experiments were carried out in C_6D_6 at 70°C with 6 mol% of Ta. **MAT-1** (■), **MAT-2** (●), **MAT-3** (▲), [(≡SiO)$_2$TaH] (⬣). **1-s** is inactive under these conditions.

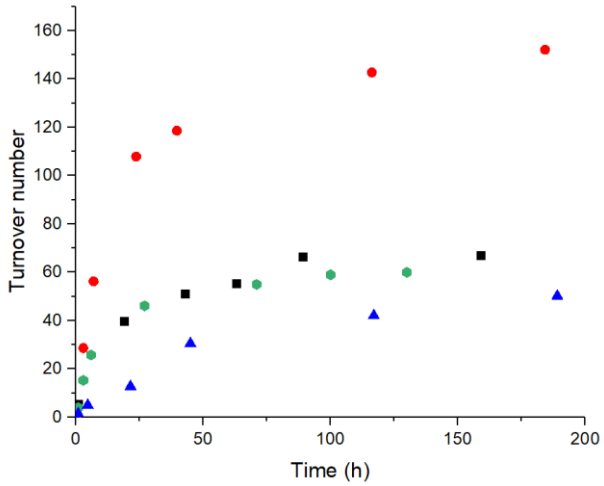

Figure 3. Propane metathesis at 200°C in batch reactor (700 mBar, 0,2 mol% Ta). **MAT-1** (■), **MAT-2** (●), **MAT-3** (▲), [(≡SiO)$_2$TaH] (⬣). TOFs determined using initial rates: **MAT-2** = 8.3 h^{-1}; **MAT-1** = 3.2 h^{-1}; **MAT-3** = 0.6 h^{-1}; [(≡SiO)$_2$TaH] = 4.4 h^{-1}.

Overall the catalytic results suggest that the active sites in **MAT-2** are different from the [≡SiOTa($CH_2{}^tBu$)$_2${IrH_2(Cp*)}] sites, **2-s**, found in **MAT-1**. In order to better understand these phenomena, molecular models were synthesized and advanced characterizations of these materials were carried out. These investigations, detailed below, support the coexistence of several surface species in **MAT-2**, and in particular the formation of bimetallic as well as trimetallic assemblies through route B as shown in Scheme 2.

3.3 Molecular models

In order to better understand the reactivity of Cp*IrH_4 towards the silica-supported tantalum alkyl alkylidene species **1-s**, we first turned our attention to molecular models. Organometallic siloxy derivatives, and in particular those belonging to the polyhedral oligomeric silsesquioxanes (POSS) family, have been used with some success as molecular models for silica-grafted species.[43,45,73–77] For instance, the silsesquioxane cage (*c*-C_5H_9)$_7Si_7O_{12}SiOH$, which mimics the isolated silanol sites found at the surface of silica dehydroxylated at 700°C, was reacted with the tantalum complex **1** to elucidate the reaction pathway leading to the surface species **1-s**.[43] In analogy with this previous study, we prepared complex {(^{i}Bu)$_7Si_7O_{12}SiO$)}Ta(CH^tBu)($CH_2{}^tBu$)$_2$, **1-POSS** and scrutinized its reactivity towards Cp*IrH_4. As shown on Scheme 3, when **1-POSS** is reacted with 0.5 equivalent of Cp*IrH_4 in C_6D_6 at room temperature, the heterobimetallic species {(^{i}Bu)$_7Si_7O_{12}SiO$)}Ta($CH_2{}^tBu$)$_2${IrH_2(Cp*)}], **2-POSS**, is obtained selectively as the sole Ir-containing species. However, when higher amounts of Cp*IrH_4 are used, a trimetallic species {(^{i}Bu)$_7Si_7O_{12}SiO$)}Ta($CH_2{}^tBu$)$_2${Ir_2H_5(Cp*)$_2$}], **3-POSS**, is formed, along with **2-POSS** and unreacted **1-POSS**. Complex **3-POSS** can be obtained quantitatively when **1-POSS** is treated with 2 equivalents Cp*IrH_4. The trimetallic aggregate **3-POSS** arises from the addition of Cp*IrH_4 onto **2-POSS**,

which competes with the addition of Cp*IrH$_4$ onto **1-POSS**. This ultimately results in the formation of a mixture of species when Ta:Ir stoichiometric ratios close to 1:1 are used (Scheme 3).

The identities of **2-POSS** and **3-POSS** were confirmed by infrared spectroscopy, ^{1}H and ^{13}C solution NMR as well as by X-ray diffraction studies. The ^{1}H-NMR spectrum for **2-POSS** displays a high-field resonance corresponding to the Ir-H hydrides at δ = -11.70 ppm and two singlets at δ = 1.23 and 2.31 ppm attributed to the ^{t}Bu and Cp* moieties respectively. The introduction of the POSS ligand induces some rigidity and a loss of symmetry, as indicated by the ^{1}H resonances of the tantalum-bound methylene groups from the two neopentyl ligands (Ta-CH$_2$) appearing as two diastereotopic doublets corresponding to two protons, with distinct chemical shifts and strong $^2J_{HH}$ couplings (δ = 0.18 and 1.29 ppm, $^2J_{HH}$ = 14.2 Hz). In the case of compound **3-POSS**, the NMR spectroscopic features of the isobutyl ligands from the POSS cage as well as those of the neopentyl and Cp* ligands are similar to those of **2-POSS**. The ^{1}H NMR resonance for the hydrides in **3-POSS** appears as a singlet at δ = -11.02 corresponding from integration to five protons. This is indicative of a rapid exchange on the NMR time scale between the various hydrides at the temperature of the experiment (298 K).

Single crystals of **2-POSS** and **3-POSS** suitable for X-ray diffraction were grown from saturated HDMSO solutions stored for 24 hours at -40°C. As seen in Figure 4, the solid-state structure of **2-POSS** displays a very short Ta-Ir distance (2.350(2) Å) which is more than 0.2 Å shorter than the sum of the respective metallic radii (Ta: 1.343 Å; Ir: 1.260 Å; sum = 2.603 Å). The formal shortness ratio (FSR) is low (0.90) and suggests a strong metal-metal interaction with a multiple Ta-Ir bond order, analogous to that found in 1. Even if the hydrides could not be located in the XRD Fourier Map, their existence was confirmed by other spectroscopic methods. Moreover, hint of their presence is given by the marked tilting of the Cp* ligand with respect to the Ta-Ir bond (Cp*$_{centroid}$-Ir-Ta angle of 146(1)°), as a result of the three-legged piano-stool coordination geometry around the Ir center which is archetypal of pentamethylcyclopentadienyl iridium complexes.[78] The Ta-C$_{Np}$ and Ta-O bond lengths (average value 2.145(1) Å and 1.876(6) Å, respectively) are in the expected range for classical Ta-neopentyl and Ta-siloxy groups.[76,79,80]

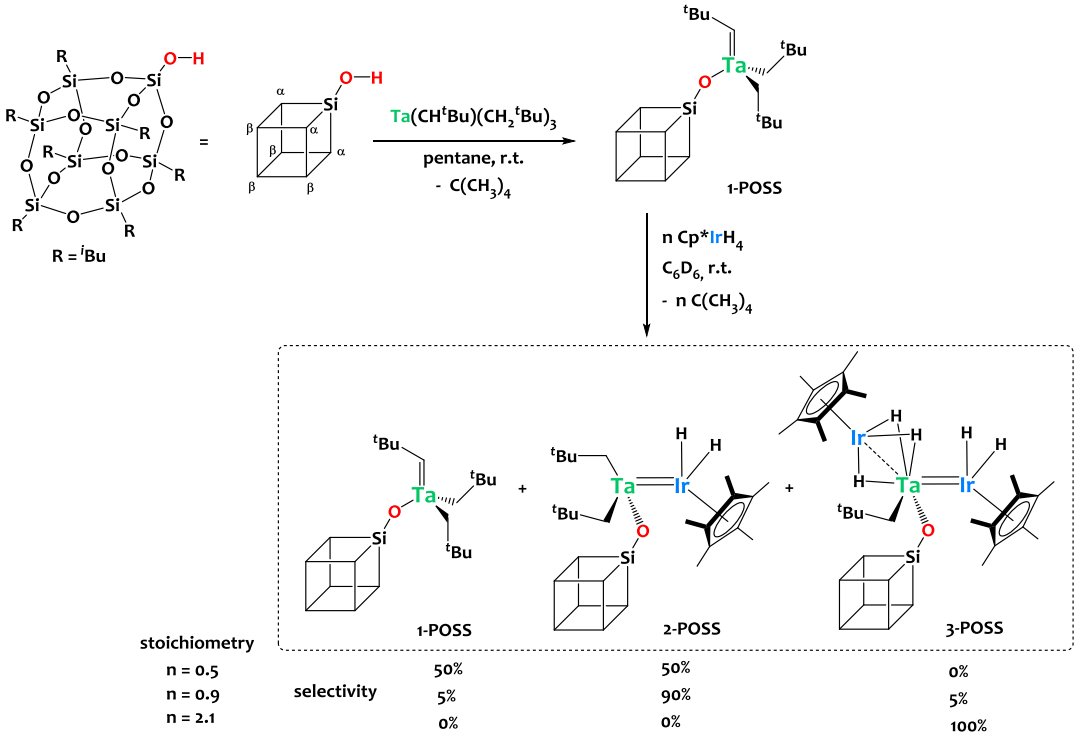

Scheme 3. Reaction of the tantalum molecular model **1-POSS** with Cp*IrH$_4$ yielding the bimetallic and trimetallic complexes **2-POSS** and **3-POSS**, respectively.

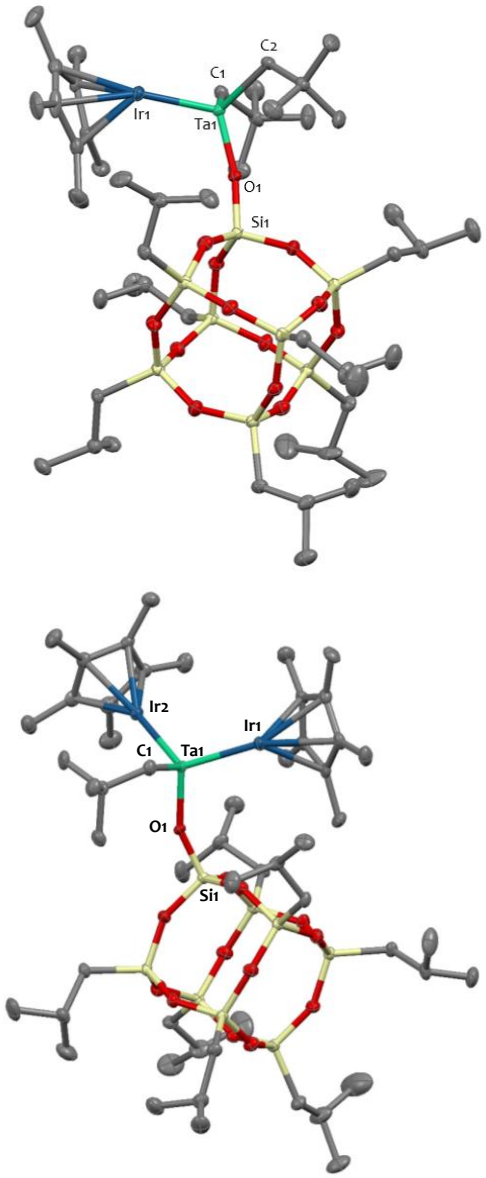

Figure 4. Solid-state molecular structures of **2-POSS** (top) and **3-POSS** (bottom) determined by X-ray diffraction. Ellipsoids are represented with 30% probability. Hydrogen atoms have been omitted for clarity. Two independent complexes are found in the asymmetric unit for **2-POSS**, only one is represented. Selected bond distances (Å) and angles (°) for **2-POSS**: Ta1-Ir1 2.350(2), Ta1-O1 1.876(6), Ta1-C_{Np} 2.15(1), Ir1-Cp*$_{centroid}$ 1.946(8), Ta1-Ir1-Cp*$_{centroid}$ 146(1), Ta1-O1-Si1 164(5). For **3-POSS**: Ta1-Ir1 2.3893(5), Ta1-Ir2 2.6113(4), Ta1-O1 1.902(5), Ta1-C2 2.185(9), Ir1-Cp*$_{centroid}$ 1.927(1), Ir2-Cp*$_{centroid}$ 1.855(1), Ta1-Ir1-Cp*$_{centroid}$ 151.38(1), Ta1-Ir2-Cp*$_{centroid}$ 177.83(1), Ir1-Ta1-Ir2 112.05(2), Ta1-O1-Si1 152.6(4).

The most striking feature of the solid-state structure of **3-POSS**, shown on Figure 4, is the disparity in the intermetallic distances and geometries. The Ta1-Ir1 distance (2.3898(5) Å) is more than 0.2 Å shorter than the Ta1-Ir2 distance (2.6113(4) Å). The Ta1-Ir1 distance displays a FSR of 0.92 and suggests the same strong metal-metal interaction with a multiple Ta1-Ir1 bond order as observed in **1** and **2-POSS**. On the contrary, the FSR for Ta1-Ir2 is slightly higher than unity (1.003) and although a direct metal-metal interaction cannot be excluded (reported Ta-Ir single bond distances span the range 2.53-2.85 Å),[81–83] the close proximity between Ta1 and Ir2 is most likely the result of the presence of bridging hydrides. The approximately linear Cp*$_{centroid}$-Ir2-Ta1 angle (177.83°) suggests the presence of 3 bridging hydrides across the two metals, arranged to favor a three-legged piano stool coordination geometry around the {Cp*Ir2} core whereas the clear tilting of the Cp* ligand with respect to the Ta1-Ir1 bond (Cp*$_{centroid}$-Ir1-Ta1 angle of 151.38°) suggests two terminal hydrides. All other metric parameters are for most part similar to those observed in **1** and **2-POSS**.

2-POSS and **3-POSS** provide good structural models for the immobilized surface heterotrimetallic complexes **2-s** and **3-s**, but equally important, **2-POSS** and **3-POSS** can serve as references to decipher the spectroscopic data recorded on the functionalized materials and corroborate the assignments proposed below.

Computational studies have been carried out at the density functional theory (DFT) level using the B3PW91 functional, to confirm the precise location of the hydride ligands (see SI), with good correlation between the crystallographic and calculated structures. The DFT analysis is also in agreement with the IR data.

Following the observation that high nuclearity systems could be formed on silsesquioxanes, we then explored the reaction between the tantalum *tris*-neopentyl neopentylidene complex Ta(CH^tBu)($CH_2{}^tBu$)$_3$ and the iridium tetrahydride complex Cp*IrH_4 in a 1:2 stoichiometric ratio. The reaction affords cleanly the trinuclear complex [{Ta($CH_2{}^tBu$)$_2$}{Ir_2H_5(Cp*)$_2$}], **3**, which is isolated in 88% yield (Scheme 4). ^{1}H NMR monitoring of the reaction in C_6D_6 solvent shows that two equivalents of neopentane are released, as expected. Evolution over time of the characteristics high field resonances of Ir-hydride protons highlights the fast formation of **2** as intermediate product (δ_{IrH} = -11.98 ppm). The latter is then slowly converted into **3** (δ_{IrH} = -10.52 ppm) by protonolysis of one Ta-neopentyl bond from **2** by an external acidic iridium-hydride from excess of Cp*IrH_4. Accordingly, the reaction of **2** with one equivalent of Cp*IrH_4 in pentane at room temperature affords quantitatively complex **3** with evolution of one equivalent of neopentane, as projected and confirmed by elemental analysis (Scheme 4).

The structure of **3** was elucidated by ^{1}H and ^{13}C solution NMR spectroscopy, infrared spectroscopy, elemental analysis and X-ray diffraction studies. The ^{1}H NMR spectrum of a solution of **3** in C_6D_6 shows three singlets at δ = 2.11, 1.33 and 0.62 ppm assigned to the Cp*, ^{t}Bu, and Ta-CH_2 moieties respectively. In addition, a single hydride resonance corresponding to five protons upon integration is observed at 298 K (singlet, δ_{IrH} = -10.52 ppm). Variable temperature ^{1}H-NMR measurements, performed in toluene-d_8 solution in the range 228-298 K, did not enable to decoalesce this resonance, indicating rapid chemical exchange on the NMR time scale between bridging and terminal hydride sites. Vibrational IR spectroscopy

exhibits a series of M-H stretching vibration signals between 2088-1968 cm^{-1}, which are assigned to Ir-H stretching vibrations. For comparison, the characteristic absorption bands of terminal iridium hydrides are 2150 cm^{-1} for Cp^*IrH_4[40], 2095 cm^{-1} for $(Cp)_2Ta(\mu\text{-}CH_2)_2Ir(SiEt_3)(H)(CO)_2$[84] and 2056 cm^{-1} for **2**,[10] Thus the broad signal distribution in complex **3** supports the concomitant presence of bridging and terminal hydrides.

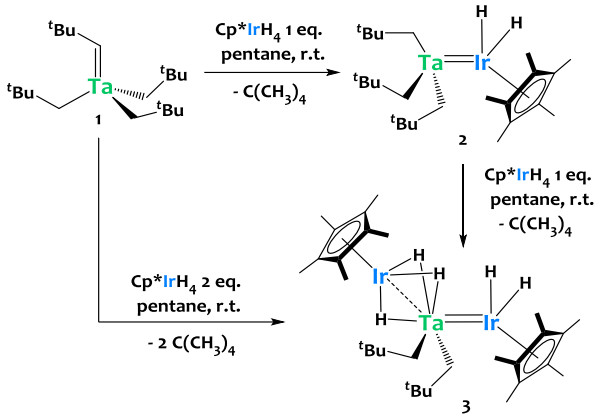

Scheme 4. Synthesis of the Ta-Ir heteropolymetallic hydride species **2** and **3** through alkane elimination.

Single crystals suitable for X-ray diffraction were grown from a saturated solution of **3** in pentane stored for 24 hours at -40°C. As for **3-POSS**, the solid-state structure of **3**, reproduced on Figure 5, displays a strong disparity in the intermetallic distances and geometries. Metric parameters for **3** and **3-POSS** are for most part similar. The formal shortness ratio for Ta-Ir1 (0.93) is in agreement with a multiple Ta-Ir1 bond and the market tilting of the Cp* ligand with respect to the Ta-Ir1 bond suggests the presence of terminal hydrides on Ir1, as observed for **3-POSS**. Conversely, the formal shortness ratio for Ta-Ir2 (0.99) indicates a weaker metal-metal bond interaction and the alignment of the Cp*centroid with the Ta-Ir2 bond suggests the presence of bridging hydrides, as confirmed by DFT studies (see SI).

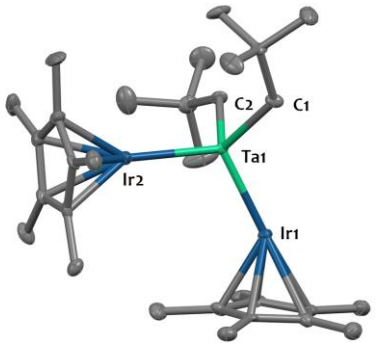

Figure 5. Solid-state molecular structure of **3** determined by X-ray diffraction. Ellipsoids are represented with 30% probability. Hydrogen atoms have been omitted for clarity. Selected bond distances (Å) and angles (°): Ta1-Ir1 2.4291(9), Ta1-Ir2 2.5891(9), Ta1-C1 2.17(2), Ta1-C2 2.18(2), Ir1-$Cp^*_{centroid}$ 1.929(1), Ir2-$Cp^*_{centroid}$ 1.857(1), Ta1-Ir1-$Cp^*_{centroid}$ 156.16(1), Ta1-Ir2-$Cp^*_{centroid}$ 178.93(1), Ir1-Ta1-Ir2 113.57(2).

3.4 Rational preparation of heterotrimetallic Ta/Ir_2 surface species

The isolation of **3** offers a unique entry point towards the clean preparation of well-defined trimetallic surface species. In order to anticipate the reactivity of **3** with silica, we investigated first the protonolysis reaction of **3** with *tris*(tert-butoxy)silanol. The reaction is carried out in a 1:1 stoichiometric ratio in pentane at room temperature and affords exclusively the monosiloxy heterotrimetallic complex **3-TBS** $[\{IrH_3(Cp^*)\}\{Ta(CH_2{}^tBu)(OSi(O^tBu)_3)_2\}\{IrH_2(Cp^*)\}]$ (Scheme 5). ^1H NMR reaction monitoring shows that 1.0 equiv. of neopentane is released in the course of the reaction, as expected. The spectroscopic and structural features of **3-TBS** closely match those of **3-POSS** (see SI).

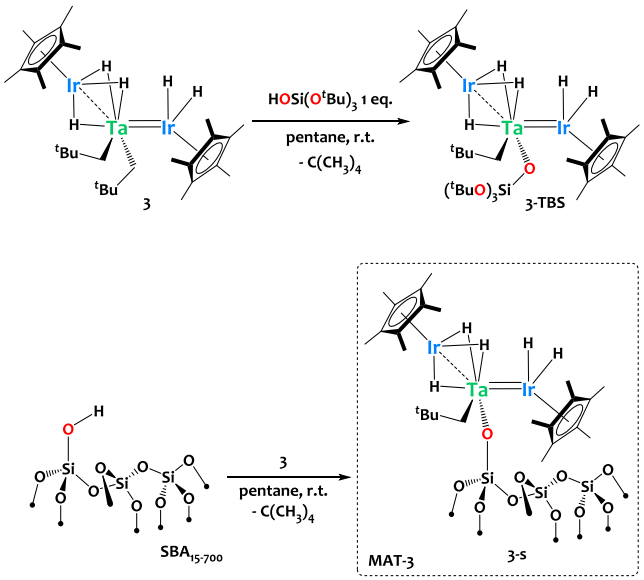

Scheme 5. Protonolysis reactivity of complex **3**.

The clean protonolysis reaction occurring with **3** led us consider the covalent grafting of **3** onto silica. Upon treatment of $SBA\text{-}15_{700}$ with a pentane solution of **3** at room temperature, the powder turns immediately yellow and 0.9 equiv. of neopentane is evolved *per* grafted Ta, as quantified by GC. DRIFT spectroscopy analysis of the resulting material, noted **MAT-3**, shows that the ν(O-H) signal at 3747 cm^{-1} assigned to isolated silanols disappears, indicating the full consumption of the isolated surface silanols through grafting, while new signals attributed to ν(C-H) stretches of the neopentyl and Cp* ligands at 2960-2860 cm^{-1} and signals assigned to ν(Ir-H) stretches at 2020 and 1947 cm^{-1} appear. The elemental analysis of **MAT-3** is in excellent agreement with the proposed formula (expected %C 10.84, %H 1.67 %Ir 13.88 %Ta 6.53; found %C 11.12, %H 1.79 %Ir 13.80 %Ta 6.45).

These analyses are consistent with the chemical grafting of the precursor onto silica *via* protonolysis of one Ta-Np bond by a surface silanol group, yielding a monopodal surface species **3-s** (Scheme 5).

Materials **MAT-1**, **MAT-2** and **MAT-3** were then subjected to advanced characterization to uncover the structural identity of their Ta/Ir surface sites.

3.5 Infrared Spectroscopy

Substantial disparities are found in the ν(Ir-H) vibrational signatures of **MAT-1**, **MAT-2** and **MAT-3** (Figure 6a). The ν(Ir-H) signal of **MAT-1** shows two bands at 2037 and 2064 cm^{-1} and is clearly different from that of **MAT-3**, which is more complex and spans a larger wavenumbers range (2020-1947 cm^{-1}). The higher number of Ir-H stretches in **MAT-3** is in adequation with its more complex structure, featuring both bridging and terminal hydrides. These IR spectra differences parallel those for the molecular analogues **2-POSS** *vs* **3-POSS** described above. Remarkably, the ν(Ir-H) signature recorded for **MAT-2** (Figure 6a) appears as a linear combination of that for **MAT-1** and **MAT-3**. This clearly indicates that route A and route B lead to different surface hydride species, and suggests that a mixture of heterobimetallic (**2-s**) and heterotrimetallic (**3-s**) surface species is present in **MAT-2**, in agreement with what is observed with the molecular models chemistry.

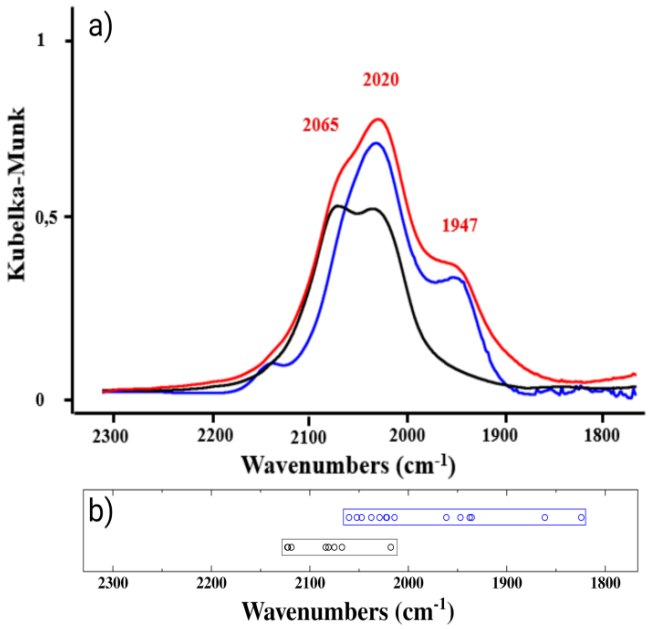

Figure 6. a) Diffuse reflection infrared Fourier transform spectra (Ir-H stretching region) of materials **MAT-1** (black line), **MAT-2** (red line) and **MAT-3** (blue line) recorded on powder materials under argon. The SBA-15_{700} signal has been subtracted to remove contribution from the support. b) Calculated Ir–H vibrational frequencies of IR-active normal mode of vibrations for **MAT-1** (black) and **MAT-3** (blue).

In Figure 6b are reported all the calculated Ir–H vibrational frequencies of IR-active normal mode of vibrations for different optimized rotamers of **MAT-1** and **MAT-3**. In **MAT-1** and **MAT-3**. There are respectively two and five distinct ν(Ir-H) normal modes, one *per* Ir-H bond. In **MAT-1**, the Ir-H stretching modes lie between 2122 and 2017 cm^{-1}, independently of the considered rotamer. In **MAT-3**, the vibrational domain is slightly shifted to lower-frequency (2060– 1824 cm^{-1}). Thus, these results make also a case for the presence of heterobimetallic (**2-s**) and heterotrimetallic (**3-s**) surface species in **MAT-2**. It is interesting to note that the M-H stretching frequencies are directly correlated with the length of the Ir-H bonds.

3.6 Solid-state NMR spectroscopy

Proton solid-state NMR spectroscopy under Magic Angle Spinning (MAS) was applied in order to further support these conclusions. The 1D ^{1}H spectra of **MAT-2** (Figure S17) and **MAT-3** (Figure S20) both display two intense signals at 2.1 and 0.9 ppm that are assigned to the CH_3(Cp*) and CH_3(Np) moieties respectively, as well as one well-defined signal at around -11.3 ppm with a small shoulder at high field corresponding to the hydride protons. The ^{13}C solid-state CP-MAS NMR spectrum of **MAT-2** shows four resonances at 110.4, 93.9, 33.5 and 9.1 ppm assigned to the *C*H_2(Np), *C*(Cp*), *C*H_3(Np) and *C*H_3(Cp*) carbons respectively (Figure S18). This NMR signature is almost identical to that observed for **MAT-3** (Figure S21), as expected as the surface species **2-s** and **3-s** bear similar organic ligands. The ^{1}H and ^{13}C NMR spectra of **MAT-1** also displayed the same set of resonances.[10] Thus, it is extremely difficult to differentiate **MAT-1**, **MAT-2** and **MAT-3** from one-dimensional solid-state NMR studies. In order to unambiguously determine the number of hydride protons attached to the metal centers and probe structural information inherent to proton-proton dipolar couplings, two-dimensional (2D) proton double-quantum (DQ) and triple-quantum (TQ) correlation spectra were recorded on **MAT-2** and **MAT-3**. These experiments enable the detection of spatial proximities between pairs (DQ) or triplets (TQ) of dipolar-coupled protons, with correlations at the sum of the individual frequencies in the indirect dimension. For hydride protons with degenerate chemical shifts, auto-correlation peaks along the $\omega_1 = 2\omega_2$ (DQ) or $\omega_1 = 3\omega_2$ (TQ) diagonal reveal the presence of pools of (at least) two or three protons respectively. The proton DQ spectra of **MAT-2** (Figure S19) and **MAT-3** (Figure S22) are similar, with auto-correlations for the CH_3(Cp*), CH_3(Np) and hydride protons. Off-diagonal correlations between the CH_3 and hydride protons are also observed. These spectra are also similar to that of **MAT-1**,[10] and do not allow one to confirm that route A and B yield different surface species. The evidence is clearly provided by proton TQ NMR spectroscopy. The SQ-TQ spectrum of **MAT-2** is shown in Figure 7. The observation of an auto-correlation along the diagonal at (−11.3 ppm, −33.9ppm) demonstrates unambiguously that 2-s is not the only species formed in route B, and that additional organometallic complexes bearing a higher number of hydrides are present. While this correlation was absent from the SQ-TQ spectrum of **MAT-1**,[10] it is clearly visible in the spectrum of **MAT-3** (Figure S23), supporting the presence of both heterobi- and heterotrimetallic surface species in **MAT-2**. A color code has been added in Figure 7 to facilitate its interpretation considering the presence of both **2-s** and **3-s**. The elongated shape of the autocorrelation indicates that the broadening of

the hydride resonance is inhomogeneous, *i.e.* corresponds to a distribution of chemical shifts due to slight structural heterogeneity likely originating from the support. We also note that fast exchange on the NMR time scale between hydrides is very likely to occur, leading to the observation of a distribution of average chemical shifts.

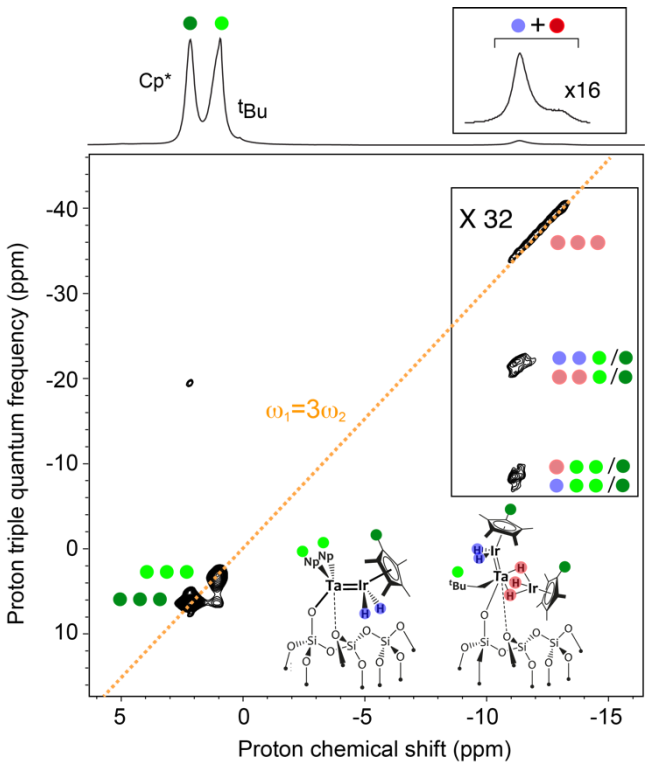

Figure 7. Proton SQ-TQ NMR spectrum (700 MHz, 2.5 mm probe, 18 kHz MAS frequency) of **MAT-2**. A total of 300 t_1 increments of 8.3 µs with 96 scans each were recorded. The total experimental time was 16 h. The trace above the 2D plot corresponds to the one-dimensional ^{1}H NMR spectrum. The dotted orange line corresponds to the $\omega_1=3\omega_2$ diagonal. The spectrum has been zoomed by a factor 32 in the hydride region to clearly show the autocorrelation at around (−11.3 ppm, −33.9 ppm). The correlations between the hydride and CH_3(Np) and CH_3(Cp*) protons at around (−11.3 ppm, −21 ppm) and (−11.3 ppm, −8 ppm) are also indicated. The other experimental conditions are described in detail in section 2.4.4.

3.7 X-Ray absorption spectroscopy

We performed XAS experiments at the Ta L_{III} edge to get more insight into the local structure and oxidation states of the surface species. X-ray absorption near-edge (XANES) spectra for **MAT-1**, **MAT-2** and **MAT-3** display edge features at ca. 9880.5 eV (Figure 8-top) and are nearly identical to that of the monometallic Ta(V) surface species **1-s**, thus indicating that the oxidation state of Ta in these materials is similar. Similarly, XANES spectra for **MAT-1**, **MAT-2** and **MAT-3** recorded at the Ir L_I edge are alike (Figure 8-bottom) and thus suggest that the Ir oxidation state is comparable in all these samples.

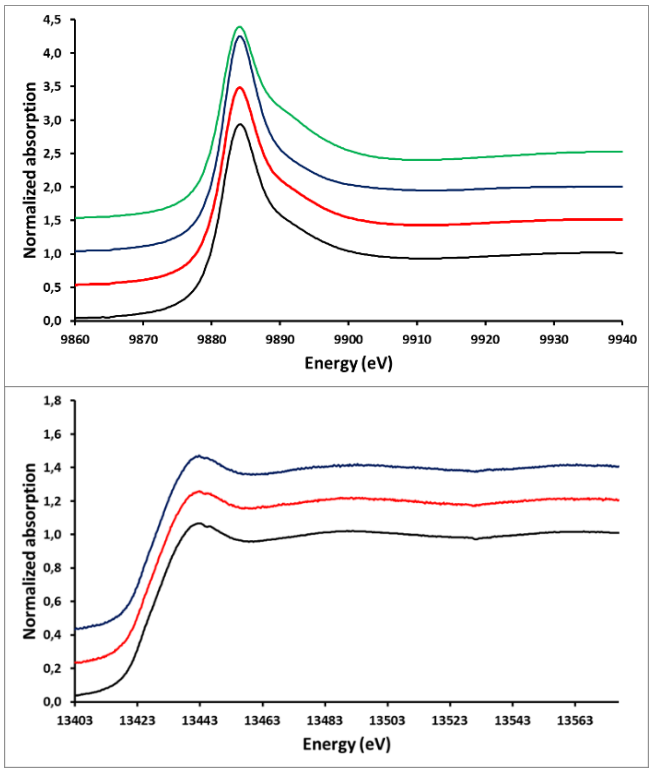

Figure 8. Ta L_{III} (top) and Ir L_I (bottom) XANES data of **MAT-1** (black line); **MAT-2** (red line); **MAT-3** (blue line) and **1-s** (green line) in *q*-space.

The results of the extended X-ray absorption fine structure (EXAFS) analysis at the Ta L_{III} edge of **MAT-1**, **MAT-2** and **MAT-3** are detailed below. Note that Ta and Ir have intertwined L-edges thus XAS measurement at the Ir L_{III} edge (11215 eV) is not feasible since it overlaps with the Ta L_{II} and Ta L_I edges (11136 and 11680 eV respectively). The Ta-O, Ta-C and Ta-Ir scattering paths used in our models correspond to the nearest neighbors around the Ta center in each sample. The amplitude of the reduction term S_0^2 (0.7) was determined using XAS data recorded on molecular complexes **2** and **3** as standards, featuring a well-known structure.

Several candidate models were considered to fit the EXAFS data at the Ta L_{III} edge of **MAT-1** (see SI). The best fit, shown in Figure 9, gives a first shell of 4 neighbors around Ta, with one oxygen atom at 1.91(1) Å, one iridium at 2.37(1) Å and two carbons at 2.05(1) and 2.18(1) Å. All these distances (Table 1) are in perfect agreement with the metrical parameters determined by X-ray crystallography on the molecular model **2-POSS** and with DFT models (Ta=Ir = 2.370 Å)[10] (see Table S1 is SI for more details). This supports the presence of **2-s** single sites at the surface of **MAT-1**. Inclusion of an additional oxygen atom in the model is detrimental to the fitting (see SI), therefore the coordination of Ta to a nearby siloxane bridge from the silica surface, as seen in other SOMC systems,[42,85] is unlikely here.

Table 1. Fitting parameters obtained from simulation of the EXAFS data of **MAT-1**.

Neighbor	N[a]	r [Å][b]	σ [Å ²][c]
O	1.2(2)	1.91(1)	0.001(1)
Ir	1*	2.37(1)	0.003(1)
C	1*	2.05(2)	0.001(1)
C	1*	2.18(2)	0.001(1)

[a] Number of neighbors. [b] Distance between the Ta center and the neighbor. [c]Debye-Waller factor. * Fixed parameters in the fit

Table 2. Fitting parameters obtained from simulation of the EXAFS data of **MAT-3.**

Neighbor	N[a]	r [Å][b]	σ [Å ²][c]
O	1.5 (3)	1.91(1)	0.002(1)
Ir	1*	2.40(1)	0.002(1)
Ir	1*	2.60(1)	0.003(1)
C	1*	2.20(2)	0.002(1)

[a] Number of neighbors. [b] Distance between the Ta center and the neighbor. [c]Debye-Waller factor. * Fixed parameters in the fit

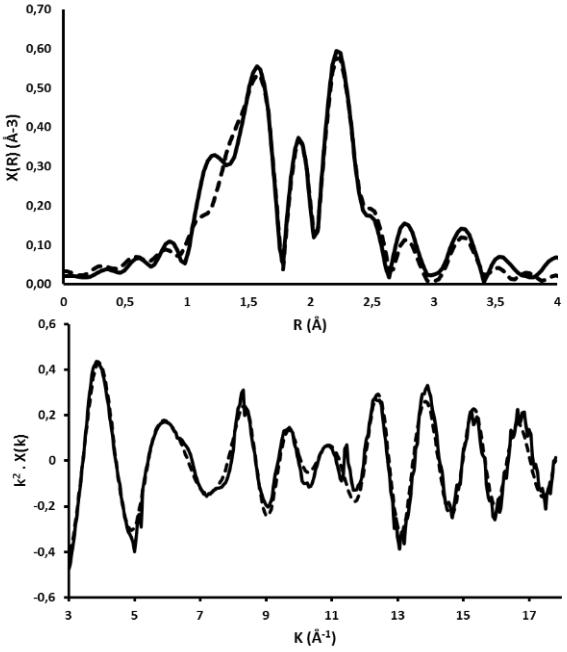

Figure 9. EXAFS Ta LIII edge experimental data (solid lines) and fit (dashed lines) of **MAT-1** in *R*-space (top) and *K*-space (bottom).

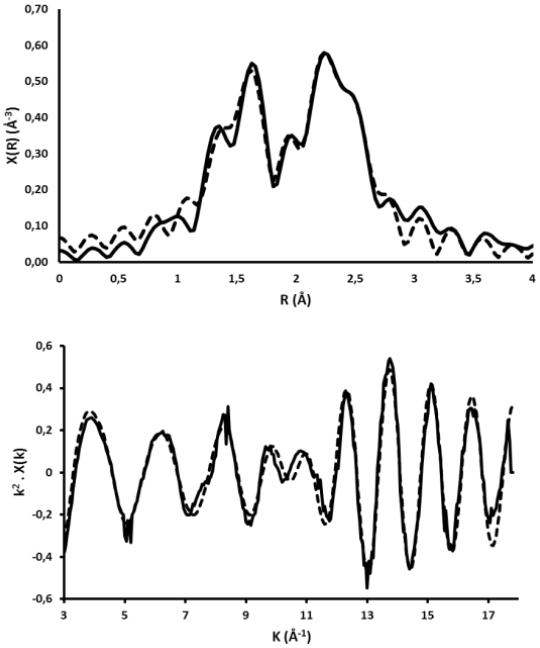

Figure 10. EXAFS Ta LIII edge experimental data (solid lines) and fit (dashed lines) of **MAT-3** in *R*-space (top) and *K*-space (bottom).

EXAFS studies performed on **MAT-3** (Figure 10) show a first shell containing two different Ir atoms (Ta-Ir1 = 2.40(1) Å; Ta-Ir2 = 2.60(1) Å), confirming the presence of a strong metal-metal interaction with a multiple Ta-Ir1 bond (FSR = 0.92) and a weaker interaction with Ir2 (FSR = 1) arising from the presence of bridging hydrides. Note that imposing two equivalent iridium atoms bound to Ta in the model, either at short (2.39(2) Å) or long (2.63(2) Å) distance, significantly worsen the EXAFS fit (see SI), which further supports the presence of two non-equivalent Ta-Ir interactions. The first coordination sphere of the Ta center is completed by about one carbon (Ta-C = 2.20(2) Å) and one oxygen (Ta-O = 1.91(1) Å) atoms. All these distances (Table 2) are again in excellent agreement with the crystal structure of the molecular analogue **3-POSS** confirming therefore the proposed structure for **3-s**.

Modelling the EXAFS data recorded for **MAT-2** using a single contribution for the calculation failed due to the poor quality of fit. To elucidate the structure of the metallic sites present at the surface of **MAT-2** we thus performed a linear combination fitting analysis of the XANES and EXAFS regions. All combinations using **1-s**, **2**, **2-s**, **3**, **3-s** and [≡SiOTa-(CH$_2$^{t}Bu)H{IrH$_2$(Cp*)}][10] data as standards were explored (see SI). Excellent fitting of the XAS data for **MAT-2** was obtained in both regions using the triple combination of **2-s** (47±7%), **3-s** (22±5%) and **1-s** (31±5%) (Figure 11). The goodness of fit factor (reduced χ^2) increases of 50%, when reducing the fit to two standards only (see SI). In light of this XAS data analysis for **MAT-2**, the contribution from the three species **1-s**, **2-s**, and **3-s** is clearly established and supports the presence of these three surface sites on **MAT-2**.

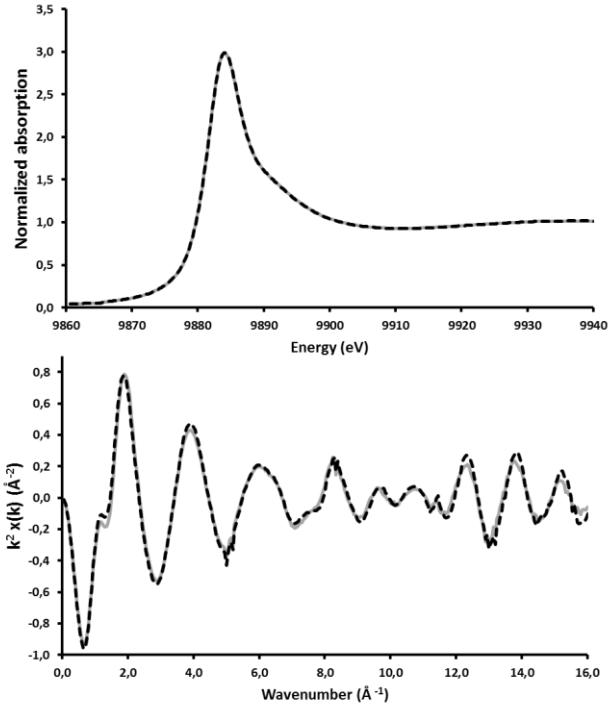

Figure 11. EXAFS Ta L_{III} edge linear combination fitting of **MAT-2** using **MAT-1**, **MAT-3** and **1-s** as standards. Experimental data (solid grey lines) and fit (dashed black lines) in *q*-space (top) and *K*-space (bottom).

Taken together, the advanced characterization of these materials through state of the art spectroscopic methods (IR, NMR and XAS):

(i) is in excellent agreement with the proposed structures for the surface species **2-s** and **3-s**,

(ii) validates the use of molecular analogues as structural models for these surface species and

(iii) supports the concomitant presence of several surface sites in **MAT-2** (**1-s** + **2-s** + **3-s**).

Strikingly, in both HIE and propane metathesis catalytic tests, the activity of **MAT-3**, which contains solely the well-defined trimetallic surface species **3-s**, is inferior to that of **MAT-2** (see Figures 2 and 3). Therefore, the enhanced catalytic activity of **MAT-2** cannot be easily explained by the sole presence of the trimetallic species **3-s**. One possible explanation is that a synergistic effect arises from the simultaneous presence of **1-s**, **2-s** and **3-s** active sites. The classically accepted reaction mechanism for alkane metathesis involves the combination of (a) an alkane dehydrogenation cycle followed by (b) an olefin metathesis cycle which redistributes the carbon chains among the transient alkene products and finally (c) a rehydrogenation step which produces the mixture of longer-chain and shorter-chain alkanes. If some of the metal surface sites described in the present work are more effective in the dehydrogenation/hydrogenation process and others are more effective in the olefin metathesis cycle then their use in combination in **MAT-2** could result in enhanced catalytic performances. Note that the cooperativity between two types of metallic sites (Zr/W and Ti/W) co-anchored on silica has been described previously and resulted in drastic improvement of the catalytic activity in propane metathesis.[19,20] Tandem alkane-dehydrogenation/olefin-metathesis systems, involving two independent metal catalysts which are not necessarily in close proximity, have also proven successful for alkane metathesis or alkane/alkene coupling.[86–89] Another hypothesis is that an unidentified minor surface species, which could not be detected despite our efforts to provide an advanced characterization of these materials, is also formed and is responsible for this increase in catalytic activity.

4. Conclusions

Different routes for the preparation of tantalum/iridium heterometallic species at the surface of SBA-15 silica dehydroxylated at 700°C have been investigated by elemental analysis, IR, advanced solid-state NMR spectroscopy, XAS, DFT computations and the synthesis of molecular models. The data are fully consistent with the formation of only one type of well-defined surface species when pre-formed bimetallic or trimetallic complexes are first prepared in solution and then grafted to the surface through the formation of a Ta-O-Si linkage. However a mixture of bimetallic (**2-s**) and trimetallic (**3-s**) species are obtained (along with some unreacted monometallic Ta sites **1-s**) using a stepwise approach which consists in exploiting the reactivity of a Ta organometallic site pre-grafted on silica with a Ir hydride complex. Quite strikingly, the material featuring both bimetallic and trimetallic sites (**MAT-2**) outperforms those featuring only one type of site in H/D exchange and alkane metathesis catalytic transformations. It is still unclear at the moment if this rise in activity is due to synergistic effects between the three types of metallic sites at the surface of the material (**1-s** + **2-s** + **3-s**), or if additional surface active species, which could not be detected despite our efforts to provide an advanced characterization of these materials, are also formed and are responsible for this increase in catalytic performances.

This study highlights the importance of the synthetic methodology used for the preparation of heterobimetallic species through SOMC, and the difficulty to obtain true single-sites.[90] It also points out a paradox: ill-defined species are often not desired since, due to their more complex nature, they are difficult to comprehend and rationalize; but at the same time, these species should not systematically be disregarded since they can have better catalytic performances. Efforts devoted to the understanding of these complex systems often paves the way to unexpected discoveries.

Declaration of Competing Interest

The authors declare that they have no known competing financial interests or personal relationships that could have appeared to influence the work reported in this paper.

Acknowledgements

We thank the "Centre de diffractométrie Henri Longchambon, Université de Lyon", and in particular Erwan Jeanneau for the single-crystal X-ray diffraction analyses. We acknowledge SOLEIL for provision of synchrotron radiation facilities and the beamline SAMBA staff for assistance. We thank Tanya K. Todorova for helpful discussions. L.M. is member of the Institut Universitaire de France. We gratefully acknowledge financial support from the "Programme Avenir Lyon Saint-Etienne de l'Université de Lyon", as part of the "Investissements d'Avenir" program (ANR-11-IDEX-0007), the CNRS-MOMENTUM 2017 program, the TGIR-RMN-THC Fr3050 CNRS and SOLEIL synchrotron (SAMBA beamline, proposal 20181971). This work was performed using HPC resources from CALMIP (Grant 2016-p0833).

Appendix A. Supplementary material

Supplementary data to this article can be found online.

References

[1] P. Buchwalter, J. Rosé, P. Braunstein, Multimetallic Catalysis Based on Heterometallic Complexes and Clusters, Chem. Rev. 115 (2015) 28–126. https://doi.org/10.1021/cr500208k.

[2] M. Sankar, N. Dimitratos, P.J. Miedziak, P.P. Wells, C.J. Kiely, G.J. Hutchings, Designing bimetallic catalysts for a green and sustainable future., Chem. Soc. Rev. 41 (2012) 8099–139. https://doi.org/10.1039/c2cs35296f.

[3] I.G. Powers, C. Uyeda, Metal-Metal Bonds in Catalysis, ACS Catal. 7 (2017) 936–958. https://doi.org/10.1021/acscatal.6b02692.

[4] N.P. Mankad, Diverse bimetallic mechanisms emerging from transition metal Lewis acid/base pairs: development of co-catalysis with metal carbenes and metal carbonyl anions, Chem. Commun. 54 (2018) 1291–1302. https://doi.org/10.1039/C7CC09675E.

[5] B.G. Cooper, J.W. Napoline, C.M. Thomas, Catalytic Applications of Early/Late Heterobimetallic Complexes, Catal. Rev. 54 (2012) 1–40. https://doi.org/10.1080/01614940.2012.619931.

[6] R. Ferrando, J. Jellinek, R. L. Johnston, Nanoalloys: From Theory to Applications of Alloy Clusters and Nanoparticles, Chem. Rev. 108 (2008) 845–910. https://doi.org/10.1021/cr040090g.

[7] D.M. Alonso, S.G. Wettstein, J.A. Dumesic, Bimetallic catalysts for upgrading of biomass to fuels and chemicals, Chem. Soc. Rev. 41 (2012) 8075–8098. https://doi.org/10.1039/c2cs35188a.

[8] R.C. Cammarota, L.J. Clouston, C.C. Lu, Leveraging molecular metal–support interactions for H2 and N2 activation, Coord. Chem. Rev. 334 (2017) 100–111. https://doi.org/10.1016/j.ccr.2016.06.014.

[9] J.A. Mata, F.E. Hahn, E. Peris, Heterometallic complexes, tandem catalysis and catalytic cooperativity, Chem. Sci. 5 (2014) 1723–1732. https://doi.org/10.1039/c3sc53126k.

[10] S. Lassalle, R. Jabbour, P. Schiltz, P. Berruyer, T.K. Todorova, L. Veyre, D. Gajan, A. Lesage, C. Thieuleux, C. Camp, Metal–Metal Synergy in Well-Defined Surface Tantalum–Iridium Heterobimetallic Catalysts for H/D Exchange Reactions, J. Am. Chem. Soc. 141 (2019) 19321–19335. https://doi.org/10.1021/jacs.9b08311.

[11] C. Copéret, A. Comas-Vives, M.P. Conley, D.P. Estes, A. Fedorov, V. Mougel, H. Nagae, F. Núñez-Zarur, P.A. Zhizhko, Surface Organometallic and Coordination Chemistry toward Single-Site Heterogeneous Catalysts: Strategies, Methods, Structures, and Activities, Chem. Rev. 116 (2016) 323–421. https://doi.org/10.1021/acs.chemrev.5b00373.

[12] C. Copéret, M. Chabanas, R. Petroff Saint-Arroman, J.-M. Basset, Homogeneous and heterogeneous catalysis: bridging the gap through surface organometallic chemistry., Angew. Chemie Int. Ed. 42 (2003) 156–181. https://doi.org/10.1002/anie.200390072.

[13] K. Weiss, W. Guthmann, M. Denzner, Investigation of polymerisation and metathesis reactions. Part XIII1 1 Part XII, K. Weiss, R. Goller and G. Lössei, J. Mol. Catal., 46 (1988) 267.: Heterogeneous bimetallic metathesis catalysts by reactions of differently substituted Fischer-type tungsten, J. Mol. Catal. 46 (1988) 341–349. https://doi.org/10.1016/0304-5102(88)85106-X.

[14] K. Weiss, M. Denzner, Untersuchungen von Polymerisations- und Metathese-Reaktionen, J. Organomet. Chem. 355 (1988) 273–280. https://doi.org/10.1016/0022-328X(88)89029-6.

[15] K. Weiss, W. Guthmann, S. Maisuls, Heterogeneous, Bimetallic Metathesis Catalysts by Reaction of Fischer-type Carbene Complexes with Reduced Phillips Catalyst, Angew. Chemie Int. Ed. 27 (1988) 275–277. https://doi.org/10.1002/anie.198802751.

[16] F. Rataboul, C. Copéret, L. Lefort, A. De Mallmann, J. Thivolle-Cazat, J.M. Basset, Synthesis, characterization and propane metathesis activity of a tantalum-hydride prepared on high surface area "silica supported zirconium hydroxide," J. Chem. Soc. Dalt. Trans. 9 (2007) 923–927. https://doi.org/10.1039/b616921j.

[17] G.L. Rice, S.L. Scott, Nonhydrolytic Surface Synthesis of a Heterobimetallic V−Ti Alkoxide Complex on Silica, Chem. Mater. 10 (1998) 620–625. https://doi.org/10.1021/cm9706199.

[18] I.B. Moroz, P. Florian, J. Viger-Gravel, C.P. Gordon, A. Lesage, C. Copéret, Silica-Grafted Tris(neopentyl)aluminum: A Monomeric Aluminum Solid Co-catalyst for Efficient Nickel-Catalyzed Ethene Dimerization, Angew. Chemie - Int. Ed. (2020) anie.202006285. https://doi.org/10.1002/anie.202006285.

[19] M.K. Samantaray, S. Kavitake, N. Morlanés, E. Abou-Hamad, A. Hamieh, R. Dey, J.-M. Basset, Unearthing a Well-Defined Highly Active Bimetallic W/Ti Precatalyst Anchored on a Single Silica Surface for Metathesis of Propane, J. Am. Chem. Soc. 139 (2017) 3522–3527. https://doi.org/10.1021/jacs.6b12970.

[20] M.K. Samantaray, R. Dey, S. Kavitake, E. Abou-Hamad, A. Bendjeriou-Sedjerari, A. Hamieh, J.-M. Basset, Synergy between Two Metal Catalysts: A Highly Active Silica-Supported Bimetallic W/Zr Catalyst for Metathesis of *n* -Decane, J. Am. Chem. Soc. 138 (2016) 8595–8602. https://doi.org/10.1021/jacs.6b04307.

[21] K. Ding, D.A. Cullen, L. Zhang, Z. Cao, A.D. Roy, I.N. Ivanov, D. Cao, A general synthesis approach for supported bimetallic nanoparticles via surface inorganometallic chemistry, Science (80-.). 362 (2018) 560–564. https://doi.org/10.1126/science.aau4414.

[22] J. Camacho-Bunquin, M.S. Ferrandon, H. Sohn, A.J. Kropf, C. Yang, J. Wen, R.A. Hackler, C. Liu, G. Celik, C.L. Marshall, P.C. Stair, M. Delferro, Atomically Precise Strategy to a PtZn Alloy Nanocluster Catalyst for the Deep Dehydrogenation of n -Butane to 1,3-Butadiene, ACS Catal. 8 (2018) 10058–10063. https://doi.org/10.1021/acscatal.8b02794.

[23] L. Rochlitz, K. Searles, J. Alfke, D. Zemlyanov, O. V. Safonova, C. Copéret, Silica-supported, narrowly distributed, subnanometric Pt-Zn particles from single sites with high propane dehydrogenation performance, Chem. Sci. 11 (2020) 1549–1555. https://doi.org/10.1039/c9sc05599a.

[24] K. Searles, K.W. Chan, J.A. Mendes Burak, D. Zemlyanov, O. Safonova, C. Copéret, Highly Productive Propane Dehydrogenation Catalyst Using Silica-Supported Ga-Pt Nanoparticles Generated from Single-Sites, J. Am. Chem. Soc. 140 (2018) 11674–11679. https://doi.org/10.1021/jacs.8b05378.

[25] J. Camacho-Bunquin, M. Ferrandon, H. Sohn, D. Yang, C. Liu, P.A. Ignacio-De Leon, F.A. Perras, M. Pruski, P.C. Stair, M. Delferro, Chemoselective Hydrogenation with Supported Organoplatinum(IV) Catalyst on Zn(II)-Modified Silica, J. Am. Chem. Soc. 140 (2018) 3940–3951. https://doi.org/10.1021/jacs.7b11981.

[26] E. Lam, G. Noh, K.W. Chan, K. Larmier, D. Lebedev, K. Searles, P. Wolf, O. V. Safonova, C. Copéret, Enhanced CH 3 OH selectivity in CO 2 hydrogenation using Cu-based catalysts generated via SOMC from Ga III single-sites, Chem. Sci. 11 (2020) 7593–7598. https://doi.org/10.1039/d0sc00465k.

[27] J.P. Candy, B. Didillon, E.L. Smith, T.B. Shay, J.M. Basset, Surface organometallic chemistry on metals: a novel and effective route to custom-designed bimetallic catalysts, J. Mol. Catal. 86 (1994) 179–204. https://doi.org/10.1016/0304-5102(93)E0211-X.

[28] W.W. Lonergan, D.G. Vlachos, J.G. Chen, Correlating extent of Pt-Ni bond formation with low-temperature hydrogenation of benzene and 1,3-butadiene over supported Pt/Ni bimetallic catalysts, J. Catal. 271 (2010) 239–250. https://doi.org/10.1016/j.jcat.2010.01.019.

[29] Q. Wang, M. Zhu, C. Xu, H. Zhang, X. Wang, B. Dai, J. Zhang, Zn-Cu bimetallic catalysts supported on pure silica MCM-41 for acetylene hydration reaction, New J. Chem. 42 (2018) 6507–6514. https://doi.org/10.1039/c8nj00707a.

[30] X. Yang, D. Chen, S. Liao, H. Song, Y. Li, Z. Fu, Y. Su, High-performance Pd-Au bimetallic catalyst with mesoporous silica nanoparticles as support and its catalysis of cinnamaldehyde hydrogenation, J. Catal. 291 (2012) 36–43. https://doi.org/10.1016/j.jcat.2012.04.003.

[31] C. Sener, T.S. Wesley, A.C. Alba-Rubio, M.D. Kumbhalkar, S.H. Hakim, F.H. Ribeiro, J.T. Miller, J.A. Dumesic, PtMo Bimetallic Catalysts Synthesized by Controlled Surface Reactions for Water Gas Shift, ACS Catal. 6 (2016) 1334–1344. https://doi.org/10.1021/acscatal.5b02028.

[32] R. Xu, K. Lian, Z. Xu, Y. Yue, P. Yuan, X. Bao, X. Yuan, H. Zhu, Controllable synthesis of Ir(Rh)-Sn/SiO2 bimetallic catalysts: Via surface organometallic chemistry for the production of ethanol from hydrogenolysis of ethyl acetate, Catal. Sci. Technol. 10 (2020) 1086–1095. https://doi.org/10.1039/c9cy02071c.

[33] Y. Zhao, K.R. Yang, Z. Wang, X. Yan, S. Cao, Y. Ye, Q. Dong, X. Zhang, J.E. Thorne, L. Jin, K.L. Materna, A. Trimpalis, H. Bai, S.C. Fakra, X. Zhong, P. Wang, X. Pan, J. Guo, M. Flytzani-Stephanopoulos, G.W. Brudvig, V.S. Batista, D. Wang, Stable iridium dinuclear heterogeneous catalysts supported on metal-oxide substrate for solar water oxidation, Proc. Natl. Acad. Sci. U. S. A. 115 (2018) 2902–2907. https://doi.org/10.1073/pnas.1722137115.

[34] Y. Yang, Y. Yang, Y. Qian, H. Li, Z. Zhang, Y. Mu, D. Do, B. Zhou, J. Dong, W. Yan, Y. Qin, L. Fang, R. Feng, J. Zhou, P. Zhang, J. Dong, G. Yu, Y. Liu, X. Zhang, X. Zhang, X. Fan, X. Fan, O-coordinated W-Mo dual-atom catalyst for pH-universal electrocatalytic hydrogen evolution, Sci. Adv. 6 (2020) 6586–6591. https://doi.org/10.1126/sciadv.aba6586.

[35] W. Ren, X. Tan, W. Yang, C. Jia, S. Xu, K. Wang, S.C. Smith, C. Zhao, Isolated Diatomic Ni-Fe Metal–Nitrogen Sites for Synergistic Electroreduction of CO2, Angew. Chemie - Int. Ed. 58 (2019) 6972–6976. https://doi.org/10.1002/anie.201901575.

[36] Z. Lu, B. Wang, Y. Hu, W. Liu, Y. Zhao, R. Yang, Z. Li, J. Luo, B. Chi, Z. Jiang, M. Li, S. Mu, S. Liao, J. Zhang, X. Sun, An Isolated Zinc–Cobalt Atomic Pair for Highly Active and Durable Oxygen Reduction, Angew. Chemie Int. Ed. 58 (2019) 2622–2626. https://doi.org/10.1002/anie.201810175.

[37] J. Wang, Z. Huang, W. Liu, C. Chang, H. Tang, Z. Li, W. Chen, C. Jia, T. Yao, S. Wei, Y. Wu, Y. Li, Design of N-Coordinated Dual-Metal Sites: A Stable and Active Pt-Free Catalyst for Acidic Oxygen Reduction Reaction, J. Am. Chem. Soc. 139 (2017) 17281–17284. https://doi.org/10.1021/jacs.7b10385.

[38] J. Zhang, Q. an Huang, J. Wang, J. Wang, J. Zhang, Y. Zhao, Supported dual-atom catalysts: Preparation, characterization, and potential applications, Chinese J. Catal. 41 (2020) 783–798. https://doi.org/10.1016/S1872-2067(20)63536-7.

[39] C.C. Hou, H.F. Wang, C. Li, Q. Xu, Q. Xu, Q. Xu, From metal-organic frameworks to single/dual-atom and cluster metal catalysts for energy applications, Energy Environ. Sci. 13 (2020) 1658–1693. https://doi.org/10.1039/c9ee04040d.

[40] T.M. Gilbert, F.J. Hollander, R.G. Bergman, (Pentamethylcyclopentadienyl)iridium Polyhydride Complexes: Synthesis of Intermediates in the Mechanism of Formation of (C5(CH3)5)IrH4 and the Preparation of Several Iridium(V) Compounds, J. Am. Chem. Soc. 107 (1985) 3508–3516. https://doi.org/10.1021/ja00298a018.

[41] R.R. Schrock, J.D. Fellmann, Multiple metal-carbon bonds. 8. Preparation, characterization, and mechanism of formation of the tantalum and niobium neopentylidene complexes, M(CH2CMe3)3(CHCMe3), J. Am. Chem. Soc. 100 (1978) 3359–3370. https://doi.org/10.1021/ja00479a019.

[42] E. Le Roux, M. Chabanas, A. Baudouin, A. de Mallmann, C. Copéret, E.A. Quadrelli, J. Thivolle-Cazat, J.-M. Basset, W. Lukens, A. Lesage, L. Emsley, G.J. Sunley, Detailed Structural Investigation of the Grafting of [Ta(CHtBu)(CH2tBu)3] and [Cp*TaMe4] on Silica Partially Dehydroxylated at 700 °C and the Activity of the Grafted Complexes toward Alkane Metathesis, J. Am. Chem. Soc. 126 (2004) 13391–13399. https://doi.org/10.1021/JA046486R.

[43] M. Chabanas, E.A. Quadrelli, B. Fenet, C. Copéret, J. Thivolle-Cazat, J.-M. Basset, A. Lesage, L. Emsley, Molecular Insight Into Surface Organometallic Chemistry Through the Combined Use of 2D HETCOR Solid-State NMR Spectroscopy and Silsesquioxane Analogues, Angew. Chemie Int. Ed. 40 (2001) 4493–4496. https://doi.org/10.1002/1521-3773(20011203)40:23<4493::aid-anie4493>3.0.co;2-x.

[44] R.J.P. Corriu, Y. Guari, A. Mehdi, C. Reyé, C. Thieuleux, L. Datas, Ordered SBA-15 mesoporous silica containing phosphonic acid groups prepared by a direct synthetic approach, Chem. Commun. 37 (2001) 763–764. https://doi.org/10.1039/b100515o.

[45] R. Duchateau, H.C.L. Abbenhuis, R.A. Van Santen, S.K.H. Thiele, M.F.H. Van Tol, Half-sandwich titanium complexes stabilized by a novel silsesquioxane ligand: soluble model systems for silica-grafted olefin polymerization catalysts, Organometallics. 17 (1998) 5222–5224. https://doi.org/10.1021/om980572g.

[46] R. Graf, D.E. Demco, J. Gottwald, S. Hafner, H.W. Spiess, Dipolar couplings and internuclear distances by double-quantum nuclear magnetic resonance spectroscopy of solids, J. Chem. Phys. 106 (1997) 885–895. https://doi.org/10.1063/1.473169.

[47] S.P. Brown, I. Schnell, J.D. Brand, K. Müllen, H.W. Spiess, An investigation of π-π packing in a columnar hexabenzocoronene by fast magic-angle spinning and double-quantum 1H solid-state NMR spectroscopy, J. Am. Chem. Soc. 121 (1999) 6712–6718. https://doi.org/10.1021/ja990637m.

[48] S.P. Brown, H.W. Spiess, Advanced solid-state NMR methods for the elucidation of structure and dynamics of molecular, macromolecular, and supramolecular systems, Chem. Rev. 101 (2001) 4125–4155. https://doi.org/10.1021/cr990132e.

[49] M. Hohwy, H.J. Jakobsen, M. Edén, M.H. Levitt, N.C. Nielsen, Broadband dipolar recoupling in the nuclear magnetic resonance of rotating solids: A compensated C7 pulse sequence, J. Chem. Phys. 108 (1998) 2686–2694. https://doi.org/10.1063/1.475661.

[50] D. Marion, M. Ikura, R. Tschudin, A. Bax, Rapid recording of 2D NMR spectra without phase cycling. Application to the study of hydrogen exchange in proteins, J. Magn. Reson. 85 (1989) 393–399. https://doi.org/10.1016/0022-2364(89)90152-2.

[51] M. Edén, M.H. Levitt, Excitation of carbon-13 triple quantum coherence in magic-angle-spinning NMR, Chem. Phys. Lett. 293 (1998) 173–179. https://doi.org/10.1016/S0009-2614(98)00761-1.

[52] M. Carravetta, J. Schmedt auf der Günne, M.H. Levitt, Enhanced triple-quantum excitation in 13C magic-angle spinning NMR, J. Magn. Reson. 162 (2003) 443–453. https://doi.org/10.1016/S1090-7807(03)00059-4.

[53] I. Schnell, A. Lupulescu, S. Hafner, D.E. Demco, H.W. Spiess, Resolution Enhancement in Multiple-Quantum MAS NMR Spectroscopy, J. Magn. Reson. 133 (1998) 61–69. https://doi.org/10.1006/jmre.1998.1432.

[54] I. Schnell, W.H. Spiess, High-resolution 1H NMR spectroscopy in the solid state: Very fast sample rotation and multiple-quantum coherences, J. Magn. Reson. 151 (2001) 153–227. https://doi.org/10.1006/jmre.2001.2336.

[55] D.F. Shantz, J. Schmedt Auf Der Günne, H. Koller, R.F. Lobo, Multiple-quantum 1 H MAS NMR studies of defect sites in as-made all- silica ZSM-12 zeolite, J. Am. Chem. Soc. 122 (2000) 6659–6663. https://doi.org/10.1021/ja000374s.

[56] B. Ravel, M. Newville, ATHENA, ARTEMIS, HEPHAESTUS: Data analysis for X-ray absorption spectroscopy using IFEFFIT, J. Synchrotron Radiat. 12 (2005) 537–541. https://doi.org/10.1107/S0909049505012719.

[57] M.J. Frisch, G.W. Trucks, H.B. Schlegel, G.E. Scuseria, M.A. Robb, J.R. Cheeseman, G. Scalmani, V. Barone, B. Mennucci, G.A. Petersson, H. Nakatsuji, M. Caricato, X. Li, H.P. Hratchian, A.F. Izmaylov, J. Bloino, G. Zheng, J.L. Sonnenberg, M. Had, D.J. Fox, Gaussian 09, (2013).

[58] J.P. Perdew, J.A. Chevary, S.H. Vosko, K.A. Jackson, M.R. Pederson, D.J. Singh, C. Fiolhais, Atoms, molecules, solids, and surfaces: Applications of the generalized gradient approximation for exchange and correlation, Phys. Rev. B. 46 (1992) 6671–6687. https://doi.org/10.1103/PhysRevB.46.6671.

[59] A.D. Becke, Density-functional thermochemistry. III. The role of exact exchange, J. Chem. Phys. 98 (1993) 5648–5652. https://doi.org/10.1063/1.464913.

[60] D. Andrae, U. Häußermann, M. Dolg, H. Stoll, H. Preuß, Energy-adjusted ab initio pseudopotentials for the second and third row transition elements, Theor. Chim. Acta. 77 (1990) 123–141. https://doi.org/10.1007/BF01114537.

[61] A. Bergner, M. Dolg, W. Küchle, H. Stoll, H. Preuß, Ab initio energy-adjusted pseudopotentials for elements of groups 13-17, Mol. Phys. 80 (1993) 1431–1441. https://doi.org/10.1080/00268979300103121.

[62] A.W. Ehlers, M. Böhme, S. Dapprich, A. Gobbi, A. Höllwarth, V. Jonas, K.F. Köhler, R. Stegmann, A. Veldkamp, G. Frenking, A set of f-polarization functions for pseudo-potential basis sets of the transition metals ScCu, YAg and LaAu, Chem. Phys. Lett. 208 (1993) 111–114. https://doi.org/10.1016/0009-2614(93)80086-5.

[63] P.C. Hariharan, J.A. Pople, The influence of polarization functions on molecular orbital hydrogenation energies, Theor. Chim. Acta. 28 (1973) 213–222. https://doi.org/10.1007/BF00533485.

[64] M.M. Francl, W.J. Pietro, W.J. Hehre, J.S. Binkley, M.S. Gordon, D.J. DeFrees, J.A. Pople, Self-consistent molecular orbital methods. XXIII. A polarization-type basis set for second-row elements, J. Chem. Phys. 77 (1982) 3654–3665. https://doi.org/10.1063/1.444267.

[65] W.J. Hehre, K. Ditchfield, J.A. Pople, Self-consistent molecular orbital methods. XII. Further extensions of gaussian-type basis sets for use in molecular orbital studies of organic molecules, J. Chem. Phys. 56 (1972) 2257–2261. https://doi.org/10.1063/1.1677527.

[66] R. Ditchfield, W.J. Hehre, J.A. Pople, Self-consistent molecular-orbital methods. IX. An extended gaussian-type basis for molecular-orbital studies of organic molecules, J. Chem. Phys. 54 (1971) 720–723. https://doi.org/10.1063/1.1674902.

[67] K.K. Irikura, R.D. Johnson, R.N. Kacker, Uncertainties in scaling factors for ab initio vibrational frequencies, J. Phys. Chem. A. 109 (2005) 8430–8437. https://doi.org/10.1021/jp052793n.

[68] M. Oishi, M. Kino, M. Saso, M. Oshima, H. Suzuki, Early − Late Heterobimetallic Complexes with a Ta − Ir Multiple Bond :, Organometallics. 31 (2012) 4658–4661.

[69] M.J. Hostetler, M.D. Butts, R.G. Bergman, Rate and Equilibrium Study of the Reversible Oxidative Addition of silanes, Organometallics. 12 (1993) 65–75.

[70] V. Vidal, A. Theolier, J. Thivolle-Cazat, J.-M. Basset, Metathesis of Alkanes Catalyzed by Silica-Supported Transition Metal Hydrides, Science (80-.). 276 (1997) 99–102. https://doi.org/10.1126/science.276.5309.99.

[71] J.-M. Basset, C. Coperet, D. Soulivong, M. Taoufik, J.T. Cazat, Metathesis of Alkanes and Related Reactions, Acc. Chem. Res. 43 (2010) 323–334. https://doi.org/10.1021/ar900203a.

[72] C. Copéret, O. Maury, J. Thivolle-Cazat, J.-M. Basset, sigma-Bond Metathesis of Alkanes on a Silica-Supported Tantalum(V) Alkyl Alkylidene Complex: First Evidence for Alkane Cross-Metathesis We are grateful to Dr. L. Lefort (LCOMS) and Dr. B. Maunders (BP Chemicals) for fruitful discussions. We also wish to t, Angew. Chemie - Int. Ed. 40 (2001) 2331–2334. http://www.ncbi.nlm.nih.gov/pubmed/11433512 (accessed December 12, 2014).

[73] E.A. Quadrelli, J.-M. Basset, On silsesquioxanes' accuracy as molecular models for silica-grafted complexes in heterogeneous catalysis, Coord. Chem. Rev. 254 (2010) 707–728. https://doi.org/10.1016/j.ccr.2009.09.031.

[74] F.J. Feher, R.L. Blanski, Olefin Polymerization by Vanadium-Containing Silsesquioxanes: Synthesis of a Dialkyl-Oxo-Vanadium(V) Complex That Initiates Ethylene Polymerization, J. Am. Chem. Soc. 114 (1992) 5886–5887. https://doi.org/10.1021/ja00040a076.

[75] M. Chabanas, A. Baudouin, C. Copéret, J.M. Basset, W. Lukens, A. Lesage, S. Hediger, L. Emsley, Perhydrocarbyl ReVII complexes: Comparison of molecular and surface complexes, J. Am. Chem. Soc. 125 (2003) 492–504. https://doi.org/10.1021/ja020136s.

[76] R. Srivastava, E.A. Quadrelli, C. Camp, Lability of Ta-NHC adducts as a synthetic route towards heterobimetallic Ta/Rh complexes, Dalton Trans. 49 (2020) 3120–3128. https://doi.org/10.1039/d0dt00344a.

[77] C. Camp, C.E. Kefalidis, J. Pécaut, L. Maron, M. Mazzanti, Controlled Thermolysis of Uranium (Alkoxy)siloxy Complexes: A Route to Polymetallic Complexes of Low-Valent Uranium, Angew. Chemie - Int. Ed. 52 (2013) 12646–12650. https://doi.org/10.1002/anie.201307291.

[78] T.M. Gilbert, R.G. Bergman, Synthesis of Trimethylphosphine-Substituted (Pentamethylcyclopentadienyl)iridium Hydride Complexes; Protonation and Deprotonation of (C5(CH3)5)Ir(P(CH3)3)H2, J. Am. Chem. Soc. 107 (1985) 3502–3507. https://doi.org/10.1021/ja00298a017.

[79] R. Srivastava, R. Moneuse, J. Petit, P.-A.A. Pavard, V. Dardun, M. Rivat, P. Schiltz, M. Solari, E. Jeanneau, L. Veyre, C. Thieuleux, E.A. Quadrelli, C. Camp, Early/Late Heterobimetallic Tantalum/Rhodium Species Assembled Through a Novel Bifunctional NHC-OH Ligand, Chem. - A Eur. J. 24 (2018) 4361–4370. https://doi.org/10.1002/chem.201705507.

[80] R.E. LaPointe, P.T. Wolczanski, G.D. Van Duyne, Tantalum organometallics containing bulky oxy donors: utilization of tri-tert-butylsiloxide and 9-oxytriptycene, Organometallics. 4 (1985) 1810–1818. https://doi.org/10.1021/om00129a022.

[81] P.L. Dunn, E.P. Beaumier, I.A. Tonks, Synthesis and characterization of tantalum-based early-late heterobimetallic complexes supported by 2-(diphenylphosphino)pyrrolide ligands, Polyhedron. 181 (2020) 114471. https://doi.org/10.1016/j.poly.2020.114471.

[82] K. Yamamoto, K. Higashida, H. Nagae, H. Tsurugi, K. Mashima, Synthesis and Characterization of Heterobimetallic Tantalum–Rhodium and Tantalum–Iridium Complexes Connected by a Tantalacyclopentadiene Fragment, Helv. Chim. Acta. 99 (2016) 848–858. https://doi.org/10.1002/hlca.201600180.

[83] M.J. Hostetler, R.G. Bergman, Synthesis and Reactivity of Cp2Ta(CH2)2lr(CO)2: An Early-Late Heterobimetallic Complex That Catalytically Hydrogenates, Isomerizes, and Hydrosilates Alkenes, J. Am. Chem. Soc. 112 (1990) 8621–8623. https://doi.org/10.1021/ja00179a078.

[84] M.J. Hostetler, M.D. Butts, R.G. Bergman, Rate and equilibrium study of the reversible oxidative addition of silanes to the iridium center in Cp2Ta(.mu.-CH2)2Ir(CO)2 and of alkene hydrosilylation/isomerization catalyzed by this system, Organometallics. 12 (1993) 65–75. https://doi.org/10.1021/om00025a015.

[85] M. Pucino, W.C. Liao, K.W. Chan, E. Lam, R. Schowner, P.A. Zhizhko, M.R. Buchmeiser, C. Copéret, Metal-Surface Interactions and Surface Heterogeneity in 'Well-Defined' Silica-Supported Alkene Metathesis Catalysts: Evidences and Consequences, Helv. Chim. Acta. 103 (2020). https://doi.org/10.1002/hlca.202000072.

[86] C.Y. Chen, D.J. O'Rear, P. Leung, Molecular redistribution and molecular averaging: Disproportionation of paraffins via bifunctional catalysis, in: Top. Catal., Springer, 2012: pp. 1344–1361. https://doi.org/10.1007/s11244-012-9910-3.

[87] M.C. Haibach, S. Kundu, M. Brookhart, A.S. Goldman, Alkane metathesis by tandem alkane-dehydrogenation-olefin-metathesis catalysis and related chemistry, Acc. Chem. Res. 45 (2012) 947–958. https://doi.org/10.1021/ar3000713.

[88] T.L. Lohr, T.J. Marks, Orthogonal tandem catalysis, Nat. Chem. 7 (2015) 477–482. https://doi.org/10.1038/nchem.2262.

[89] J.A. Labinger, D.C. Leitch, J.E. Bercaw, M.A. Deimund, M.E. Davis, Upgrading Light Hydrocarbons: A Tandem Catalytic System for Alkane/Alkene Coupling, Top. Catal. 58 (2015) 494–501. https://doi.org/10.1007/s11244-015-0380-2.

[90] D. Gajan, C. Copéret, F.X.L. i Xamena, K.A. Scheidt, S.T. Nguyen, J.T.

Hupp, B. Walaszek, G. Buntkowsky, H.H. Limbach, B. Chaudret, R.A. Fischer, L. Veyre, G. Bodenhausen, C. Copéret, L. Emsley, Silica-supported single-site catalysts: to be or not to be? A conjecture on silica surfaces, New J. Chem. 35 (2011) 2403. https://doi.org/10.1039/c1nj20506d.

Graphical abstract: